

EVALUATING CONTACT ANGLE HYSTERESIS IN POROUS ROCKS BASED ON MICRO-CT IMAGING DATA

A STUDY ON PORE-SCALE FLUID DISPLACEMENTS DURING
IMBIBITION IN POROUS MEDIA

Sharon Ellman

Student number: 01911926

Promotor: Dr. Tom Bultreys

Jury: Prof. dr. Veerle Cnudde, Prof. dr. Kamaljit Singh

Master's dissertation submitted in partial fulfilment of the requirements for the degree of master in geology

Academic year: 2020-2021

Acknowledgements

“Blood, sweat and tears” (perhaps without the blood) is a good phrase to describe the hard work that goes into producing a master’s thesis. Besides this, it also takes incredible guidance and support from a multitude of people.

To my supervisor, Tom Bultreys, thank you for your patience, guidance, ever-available help and for making me feel like part of the team. You have helped fuel my love for research, especially on the topic of pore-scale fluid dynamics and have showed me how intriguing problem solving can be. To my mentor, Arjen Mascini, thank you for showing me the ropes and answering my never-ending stream of questions. Your friendliness and helpfulness made settling in to UGent easier. I could not have done this without the two of you. Your insights and guidance have helped me grow as a scholar and researcher.

To Jan Wuzyk, thank you for teaching me how to code. Your help, support and confidence in me have helped me achieve things I’ve always wanted to master. To my friends, thank you for pushing me to be the best I can be and to occasionally still “stop and smell the roses”.

To my family, you have my eternal gratitude. Your unconditional love and support have always allowed me to rise up to challenges and tackle them head on. Your unwavering faith in me has made me strive to be better, to be the person you already see me to be. Mom, Dad, thank you for everything.

The story of my research

From a young age, I was captivated by science. I spent many afternoons with my grandfather where he taught me many things, ranging from how the planets rotate around the sun to how all matter is made up of tiny particles we cannot see called 'atoms'. This meant that from early on I wanted to go into the sciences and discover new truths. This led me to pursue Geology as a field of study at university. Geology combined my love of physics, chemistry, geography and mathematics. For my bachelor's project, I did research on groundwater flow in discrete rock fractures and how this flow could be related to Bernoulli's equation. This sparked my interest in how fluids flow through media.

When I came to Ghent University, I was able to further explore my passion for groundwater and quickly became interested in the work that the PProGRes team was doing, especially related to fluid flow. The projects they were working on combined geology with physics and numerical modelling, speaking to the curiosity I had always had for multidisciplinary approaches. This led me to choose a thesis topic with Dr. Tom Bultreys, focussing on how fluids interact and propagate inside of permeable rock. Understanding this can help lessen climate change by improving CO₂ sequestration, improve groundwater resources by improving groundwater remediation and countless other uses. Part of why I chose this research topic is because I felt that it would produce results that could make a difference to our futures. Combating climate change and other problems facing our society is well worth some effort, which is why I felt this project was a good choice for me.

This research project has enabled me to learn many new skills and has made me grow as a researcher and an upcoming scientist. It posed many challenges that I had to overcome and taught me the value of hard work and perseverance. It is my wish to work towards answering the questions of the scientific community and society at large. I truly believe that the pursuit of knowledge by combining different disciplines and thinking out of the box can help solve the problems facing the world today.

Table of Contents

1. Introduction	1
2. Literature Review	2
2.1. Multiphase fluid flow	2
2.1.1. Definitions and principles	3
2.1.2. Hysteresis in multiphase flow	10
2.1.3. Contact angle hysteresis	11
2.2. State-of-the-art	12
2.2.1. Fluid displacement in two-dimensional systems.....	12
2.2.2. Three-dimensional imaging of fluid flow.....	13
2.2.3. Time-resolved fluid flow in three-dimensional systems	15
2.3. Contact angle measurements	16
2.3.1. Geometric contact angles.....	16
2.3.2. Force-based contact angles.....	17
2.3.3. Thermodynamic contact angles	17
2.3.4. Event-based contact angles.....	17
3. Materials and methods	18
3.1. X-ray CT	18
3.1.1. Basic principles	18
3.1.2. X-ray systems.....	19
3.1.3. Image quality and artefacts	20
3.1.4. Data analysis and visualization	22
3.2. Experimental dataset.....	22
3.3. Sensitivity analysis on image processing	23
3.4. Image analysis of imbibition	24
3.4.1. Identifying imbibition fluid displacement events.....	24
3.4.2. Geometric contact angles.....	26
3.4.3. Capillary pressures and force-based contact angles.....	27
3.4.4. Thermodynamic contact angles	28
3.4.5. Validation and verification	28
4. Results.....	28
4.1. Case studies of single event results	28
4.1.1. Piston-like filling	28
4.1.2. Cooperative pore filling	31
4.1.3. Snap-off.....	33
4.2. Pore filling statistics.....	34
4.2.1. Event overview	34
4.2.2. Global curvatures.....	36
4.2.3. Capillary pressures.....	36
4.2.4. Volumes and surface areas	37
4.2.5. Geometric, event-based, force-based and thermodynamic contact angles.....	38

4.3.	Comparison between imbibition and drainage	40
5.	<i>Discussion</i>	42
5.1.	Validation and verification	42
5.1.1.	Manual geometric contact angle measurements	42
5.1.2.	Event visualization	42
5.1.3.	Capillary pressures	43
5.2.	Case studies of single events	43
5.2.1.	Geometric contact angles and curvatures	43
5.2.2.	Surface areas	44
5.3.	Pore filling statistics	45
5.3.1.	Event overview	45
5.3.2.	Global curvatures and event pressures	45
5.3.3.	Comparison of different types of contact angles	46
5.4.	Comparison between imbibition and drainage	47
6.	<i>Conclusion</i>	49
	<i>References</i>	51

1. Introduction

The flow of fluids in permeable media is crucial to several pressing issues facing the world at present. An example is combatting climate change: an important approach to this global crisis is carbon dioxide capture and sequestration (CCS)^{1,2}. Geological carbon sequestration in deep saline aquifers or depleted oil and gas fields is such a method which can be used to store large volumes of CO₂ (Mt/year) and thus abate greenhouse gas emissions. This technology is inextricably linked to the simultaneous flow of multiple fluids (multiphase flow, in this case of water or brine and CO₂) in the pore space³. Another example is the growing problem of water availability. Water scarcity is becoming more and more common due to socioeconomic developments as well as due to the effects of climate change⁴. Europe has been experiencing uncharacteristically hot summers which has led to an increase in drought occurrences throughout the continent^{5,6}. This places a great importance on the fields of subsurface contaminant transport⁷ and water purification, to ensure accessible fresh water remains usable. Understanding the fluid dynamics in permeable media is therefore critical.

Fluids in the subsurface are typically found within the pore space of rocks or sediments. This is the portion of the material consisting of voids, filled with fluids. In permeable materials, (a portion of) this space is interconnected, allowing for fluids to flow through. The distributions of these fluids in the pore space have been studied in order to understand fluid displacement mechanisms, which have an important control over multiphase flow⁸⁻¹⁰. During slow fluid flow, such as that usually occurring in the subsurface, one of the most important factors controlling fluid flow dynamics is the wettability of the pore walls (solid surfaces forming the boundaries of the pore space). The wettability expresses the relative tendency of each of the fluids to cover the surface of a solid and is quantified by the angle which the fluid/fluid interface (fluid meniscus) makes with the solid surface (contact angle). This angle is hence pivotal to determining how the advancing fluid migrates through the pore space and which fluid displacement mechanisms may occur. One of the complicating factors is that contact angles are hysteretic in nature. The roughness of solid surfaces cannot be resolved at all scales. This results in an “effective” contact angle, which is the angle that the fluid/fluid interface appears to make with the solid surface. Advancing contact angles and receding contact angles are different for the same medium, meaning measurements depend on the nature of the movement of the fluids. This is due to unresolved roughness.

The standard methods to characterize wettability depend on macroscopic measurements, e.g. the contact angle of a droplet suspended from a cm-scale rock sample¹¹. Since this does not directly capture the wetting behaviour in the pores, X-ray imaging methods have been proposed to measure the contact angles at the micrometre scale, inside porous materials (e.g. rock samples). The standard approach for this has been to use all contact angles measured on the fluid-fluid-solid contact lines in a single X-ray micro-computed tomography (μ CT) image of a static fluid distribution^{12,13}. Fluid displacements, however, frequently occur as fast events, meaning this process is dynamic in nature. In order to take this dynamic nature into account when making measurements, Mascini et al.¹⁴ defined an “event-based contact angle”, using time-resolved μ CT images of drainage experiments to measure contact angles just before fluid meniscus movements (“events”). They then proposed a new contact angle measurement using fluid meniscus curvatures instead of directly measuring the geometric angle of the meniscus with the solid surface. This connects the pore-scale wettability to the capillary pressure at which fluid displacements occur, which is important to improve pore-scale models of these displacements. However, no such study has been conducted for imbibition, despite the fact that the pore-scale dynamics of this process are generally more difficult to model. Furthermore, this also leaves questions on contact angle hysteresis, especially whether and how this can be measured inside porous materials during drainage-imbibition displacements. Answering these questions

will aid in our understanding of subsurface fluid dynamics, and consequently in better pore-scale models to predict them.

In order to gain insights into the dynamics of imbibition, the first objective set in this dissertation is to assess whether it is possible to measure event-based contact angles for imbibition. We hypothesize that these will provide a more precise measure than the conventional method of measuring contact angles on static fluid distributions, because event-based measurements better account for the dynamic nature of fluid displacement. This will be tested on a publicly available time resolved μ CT dataset of fluid flow experiments on a glass bead pack⁸. Events will be identified and used to calculate the event-based contact angles. The event-based measurements will then be compared to the static methods of measurement (geometric contact angles and thermodynamic contact angles, using methods developed by AlRatrouf et al.¹³ and Blunt et al.¹⁵).

The second objective is to assess contact angle hysteresis by comparing the measurements on imbibition to those made by Mascini et al.¹⁴ on drainage of the same sample. For this, the filling event types, i.e. the different processes by which pores can be filled during imbibition, will first be identified so that a pore-by-pore comparison can be made. Hysteresis will be quantified by assessing differences in event characteristics and in mean contact angles. This will allow for a deeper understanding of fluid flow processes and how advancing and receding contact angles relate to each other.

The final objective is to determine whether force-based contact angle measurements can be determined for imbibition and whether these can be used to validate or improve pore network models. The event types will determine which method of calculating the force-based contact angle can be used. Capillary pressures will be calculated as an intermediate step in the force-based contact angle calculations. Capillary pressures determined by models and by experimental methods will be compared with each other as a form of validation.

Using event-based approaches to investigate imbibition will provide us with a deeper understanding of the dynamics involved with this process. It aims to allow for the quantification of hysteresis via methods that take the dynamic origins of hysteresis into account. Understanding these processes of fluid displacement and being able to predict how this displacement will occur, is essential to improving models of multiphase fluid flow. These models are critical for ensuring efficient subsurface storage of CO₂¹⁶ and geological energy storage¹⁷ as well as effective subsurface contaminant remediation, to name but a few examples.

2. Literature Review

In the following section, background information related to the topic of this dissertation will be put forward. A number of relevant concepts in the field of multiphase fluid flow will be discussed in the first subsection. The next subsection will discuss the state-of-the-art of the research field, with the final subsection discussing different types of contact angle measurements.

2.1. Multiphase fluid flow

Multiphase flow is the simultaneous flow of more than one fluid. In the context of this dissertation, it is the simultaneous flow of multiple fluids within the pore space. The pore space is made up of larger voids called pores, which are connected to each other via narrower voids called throats.

2.1.1. Definitions and principles

Wettability and contact angle

Wettability is an important property in multiphase flow. It refers to the tendency of a solid surface in contact with two fluids to be preferentially covered by one fluid instead of the other. The fluid which preferentially covers the solid surface is referred to as the wetting fluid, while the other is referred to as the non-wetting fluid¹⁸. As represented in Figure 1, an interfacial tension exists between the two fluids and between the solid and each fluid.

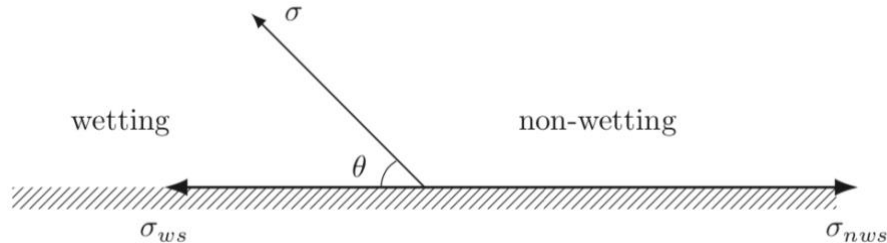


Figure 1: Diagrammatic representation of two fluids in contact with a solid surface. In reality, the fluid/fluid interface is curved, but in this case the interface has been enlarged to the point where it appears to be a straight line so as to simplify the representation. θ is the contact angle¹⁹.

The interfacial tension is the energy per unit area associated to the surface between two phases, with the unit of force/length²⁰. The balance of these determines the distribution of fluids in the presence of a solid surface¹⁵. To explain this using an example, consider the presence of water and oil (a hydrocarbon fluid consisting of non-polar molecules) on a quartz grain surface. The quartz is held together by strong inter-atomic bonds. The polar nature of water means that it will experience some electrostatic attraction to the quartz grain surface²¹. This is energetically favourable and results in a relatively low interfacial tension between the water and the quartz grain surface. The oil is only attracted to the quartz surface via weak Van der Waal's forces, resulting in a higher interfacial tension than for the water and quartz. To minimize the interfacial tensions exerted within the system, water acts as the wetting fluid, preferentially spreading across the quartz grain, while the contact area between oil and the quartz is minimised, making it the non-wetting fluid¹⁹. This yields the equation:

$$\sigma_{nws} = \sigma_{ws} + \sigma \cos\theta \quad \text{Eq. 1}$$

where σ_{nws} is the interfacial tension between the solid surface and the non-wetting fluid, σ_{ws} is the interfacial tension between the solid surface and the wetting fluid, σ is the interfacial tension between the two fluids and θ is the contact angle, which is the angle that the fluid/fluid interface makes with the solid surface¹⁹.

The contact angle, θ in Figure 1, is often used to characterise wettability. A wetting fluid means that the angle measured through the fluid is less than 90° , while a non-wetting fluid means that the angle measured through the fluid is more than 90° . By convention, the contact angle is measured through the denser of the two fluids when reporting the contact angle of a system. In Figure 2B, the illustration shows a contact angle of 45° , meaning water is the wetting fluid and oil is the non-wetting fluid. Figure 2D, on the other hand, shows a contact angle of 135° , indicating in this situation water is the non-wetting fluid, while oil is the wetting fluid. Since water is the denser fluid, the contact angles are measured through water.

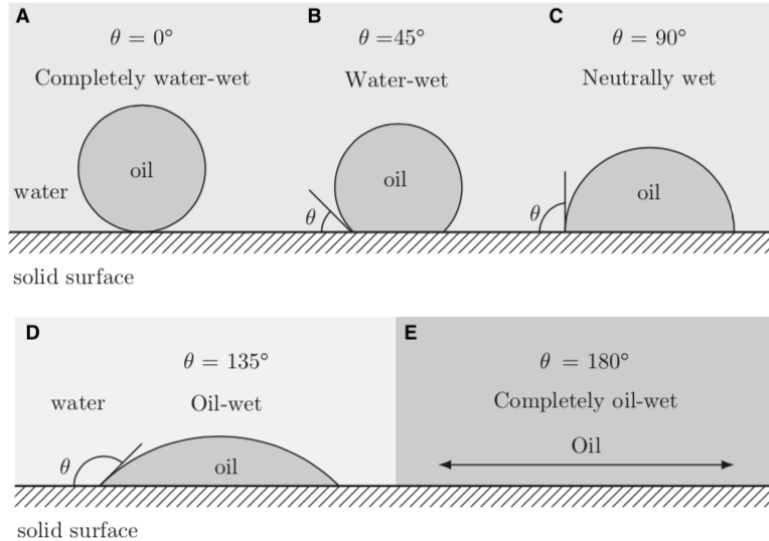


Figure 2: “Water-wet” refers to a system where water is the wetting fluid. “Oil-wet” refers to a system where oil is the wetting-fluid¹⁹.

In a confined geometry such as that seen in Figure 3, one fluid is the non-wetting fluid and is repelled from the surface, while the other is the wetting fluid and preferentially covers the surface. This causes the interface between the two fluids to be curved. One needs only to think of water rising in a capillary tube and the meniscus that is formed to visualize this phenomenon.

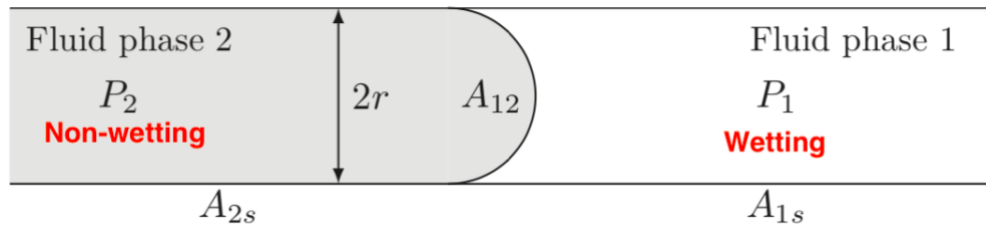


Figure 3: The non-wetting phase is bulging into the wetting phase, reducing its contact with the surface¹⁹.

Capillary pressure

Capillary pressure (P_c) arises for the same reason as wettability and contact angles do, due to the interaction of forces within fluids, between fluids and between solid surfaces and fluids²². The curvature in the fluid/fluid interface, as seen in Figure 3, is linked to a pressure difference between the two fluids. The fluid which bulges out into the other fluid is at a higher pressure. In porous media (as well as capillary tubes), it is the non-wetting fluid which bulges into the wetting fluid, ensuring the non-wetting fluid has as little contact with the surface as possible. Since the non-wetting fluid is repelled by the solid, it needs to be at a higher pressure than that of the wetting fluid to be able to intrude the pore space¹⁹.

Capillary pressure is the difference between the pressures of each fluid measured across the fluid/fluid interface. This is equal to pressures measured by external pressure transducers when fluids in the pore space are connected and are at perfect equilibrium. This yields:

$$P_c = P_{nw} - P_w \quad \text{Eq. 2}$$

where P_{nw} is the pressure within the non-wetting fluid and P_w is the pressure within the wetting fluid²².

At a microscopic scale, capillary pressure is the pressure difference at which the fluid/fluid interface remains fixed. If P_c increases or decreases, the fluid/fluid interface shifts until a new equilibrium is reached as shown

in Figure 4. The P_c at which the fluid/fluid interface moves can be referred to as the threshold capillary pressure ($P_{c,thr}$). $P_{c,thr}$ is associated with a threshold curvature (κ_{thr}) and corresponds to a specific throat radius (for drainage) or pore radius (for imbibition). The narrower the pore/throat through which the interface must move, the higher the $P_{c,thr}$. It also depends on the geometry of the pore/throat¹⁴ and is linked to the interfacial tension²³. For simplicity, the geometry is often considered to be cylindrical. This all leads to the Young-Laplace equation for capillary pressure:

$$P_{c,thr} = \sigma \left(\frac{1}{r_1} + \frac{1}{r_2} \right) \quad \text{Eq. 3}$$

$$P_{c,thr} = 2\kappa_{thr}\sigma = \frac{2\sigma \cos \theta}{r} \quad \text{Eq. 4}$$

where P_c is the capillary pressure, σ is the interfacial tension, r_1 and r_2 are the principal radii of curvature of the fluid/fluid interface, κ_{thr} is the threshold mean curvature of the fluid/fluid interface, θ is the contact angle and r is the pore/throat radius. In Eq. 4, θ would only equal the actual contact angle measured along the contact line if the pore/throat would be perfectly cylindrical in shape¹⁴. The mean curvature is calculated by taking half of the sum of the principal curvatures ($\kappa_{mean} = \frac{\kappa_1 + \kappa_2}{2}$)²³. The principal curvatures are obtained by selecting the minimum and maximum curvatures out of all possible curvatures measured through a point on the surface²³.

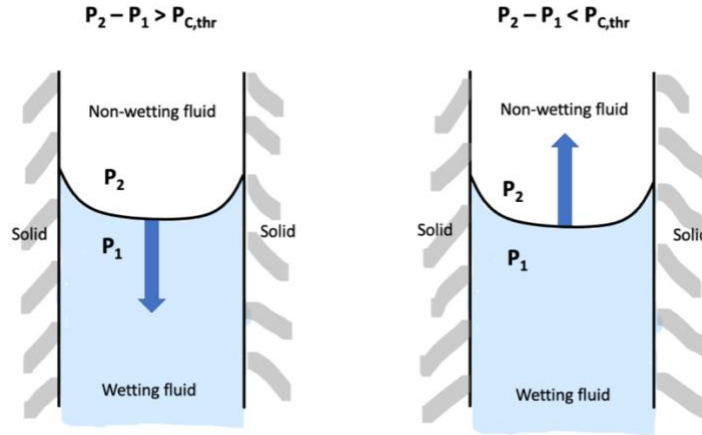


Figure 4: At the microscopic scale, if the threshold capillary pressure is exceeded, the non-wetting fluid surges forward as in the left image. If the pressure difference is less than the threshold capillary pressure, the wetting fluid moves forward, as in the right image.

Terminal and Arc menisci

A terminal meniscus is a fluid/fluid interface which straddles a pore or a throat and stops flow through its centre¹⁹. Both principal radii of curvature of these interfaces are on the scale of the throat radii. An arc meniscus is a fluid/fluid interface located in the corners of pores or throats or in roughness¹⁹. These interfaces occur when there are small brine layers along pore walls.

Drainage

Drainage is the process whereby the wetting fluid within the pore space is displaced by the non-wetting fluid. Pushing the non-wetting fluid into the pore space requires a force, hence this is not a spontaneous process¹⁹. A common example is when water in the subsurface migrates downwards under the force of

gravity and the pore space fills with air. The air is the non-wetting fluid and it displaces water, which is the wetting fluid.

Consider an experiment where the non-wetting fluid surrounds a porous material which contains wetting-fluid. According to the Young-Laplace capillary pressure equation (Eq. 4), the non-wetting fluid would be able to enter the largest spaces first¹⁹: as the capillary pressure increases, eventually the threshold capillary pressure for the largest throat will be reached and the non-wetting fluid will enter the pore space. This means that as drainage occurs, the largest throats are invaded by the non-wetting fluid first, with smaller throats only being invaded when the capillary pressure is sufficiently high.

Displacement events during drainage typically occur rapidly²⁴. They are controlled by the narrowest passages through which the interface must move, i.e. the pore throats. This process is driven either by the pressure of the non-wetting fluid increasing or the pressure of the wetting fluid decreasing, either of which cause an increase in capillary pressure. This increase in capillary pressure causes the fluid/fluid interface to bulge more and more. Eventually, when the threshold capillary pressure is reached, the interface surges forwards until it reaches the next narrowest passage. This is called a Haines jump (Figure 5). Displacement events during drainage are often piston-like displacements, with the non-wetting fluid invading the pore space as one continuous, connected cluster²⁵. Roof snap-off is another form of drainage displacement. As the fluid/fluid interface suddenly surges forwards during a Haines jump, the leading interface's curvature decreases, causing disequilibrium in different areas of the interface. If the curvature decreases to below the curvature corresponding to the snap-off capillary pressure of a throat in the proximity of the Haines jump, the leading portion of non-wetting fluid can become disconnected, forming an isolated ganglion^{26,27}.

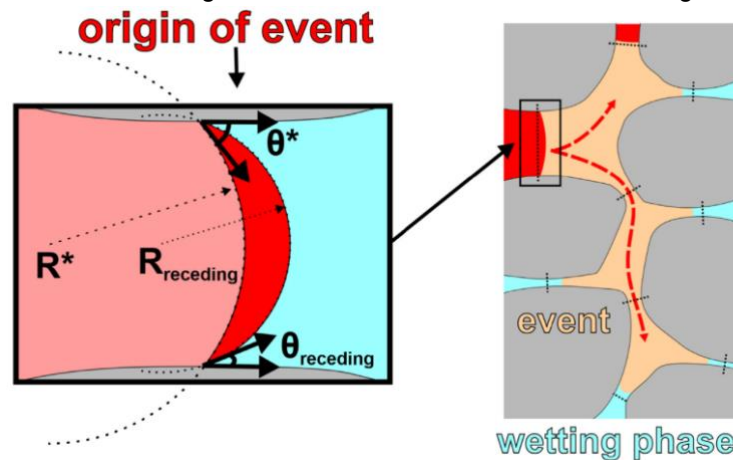


Figure 5: Diagrammatic representation of a Haines jump. As pressure builds, the interface bulges and shifts from R^* to R . When the threshold capillary pressure is reached, the interface surges forwards until the next narrowest passages are reached as in the right of the image. Figure from Mascini et al.¹⁴.

Imbibition

Imbibition can be seen as the reverse process to drainage. It is the process whereby the non-wetting fluid is displaced by the wetting fluid. Since it is the fluid which preferentially covers the surface which is now entering the pore space, this process can occur spontaneously. An everyday example is when rainwater enters the subsurface, displacing the air that was there in the pore space. In geological carbon dioxide sequestration, this process occurs when a CO_2 plume migrates along the caprock in a saline aquifer and water re-enters the tail of the plume where the CO_2 has migrated away²⁵.

Consider an experiment where the non-wetting fluid has been pumped under pressure into a porous material. By now reducing the pressure on the non-wetting fluid, imbibition can be induced. In order to optimize the energies related to the contact between the fluids and the surface, the wetting-fluid typically enters smaller pores first. This maximises the surface area to volume ratio of the wetting fluid in the porous media. The largest passages through which the fluid/fluid interface must migrate, i.e. pore bodies, are the limiting locations for this process to proceed¹⁹.

During imbibition, “fast events” (capillary instabilities) are interspersed with “slow and steady” reversible interface movements (such as film growth). Film growth typically occurs throughout the rock, meaning the volume of water that enters the rock is distributed throughout the pore space. This causes the fluid interface instabilities to be spread out through space, instead of being highly localised as is the case for drainage^{28,29}. For the sake of clarity, imbibition events are understood as capillary instabilities, which are fast occurring events, similar to the events during drainage. The distribution of the fluids within the pore space, as well as the co-ordination numbers of the pores, influence how these events occur. The co-ordination number of a pore is the number of other pores it is connected to via pore throats. The different types of imbibition events are piston-like displacement, cooperative pore filling and snap-off³⁰.

Piston-like displacement is the simplest of these event types. It involves the wetting fluid displacing the non-wetting fluid within a pore throat³⁰. This type of displacement does not change the connectivity of the system.

Cooperative pore filling occurs when the wetting fluid displaces the non-wetting fluid inside of a pore. The threshold capillary pressure for the wetting fluid to enter a pore is directly related to the threshold curvature. The curvature in turn depends on the largest possible radius of curvature that can be achieved. This is determined by the number of non-wetting fluid filled pore throats adjacent to this pore³¹. A pore which has one non-wetting fluid filled throat adjacent to it will thus have a different threshold capillary pressure than a pore which has two non-wetting fluid filled throats adjacent to it, for example. Hence, depending on the local fluid arrangement, a pore with co-ordination number z can have $z-1$ different possible types of events filling it, each occurring at a different threshold capillary pressure³⁰. The ‘ n ’ value in I_n events is determined by the number of non-wetting fluid filled throats that surround the event pore at the time it is filled (Figure 6). I_1 events are the same as piston-like pore fillings.

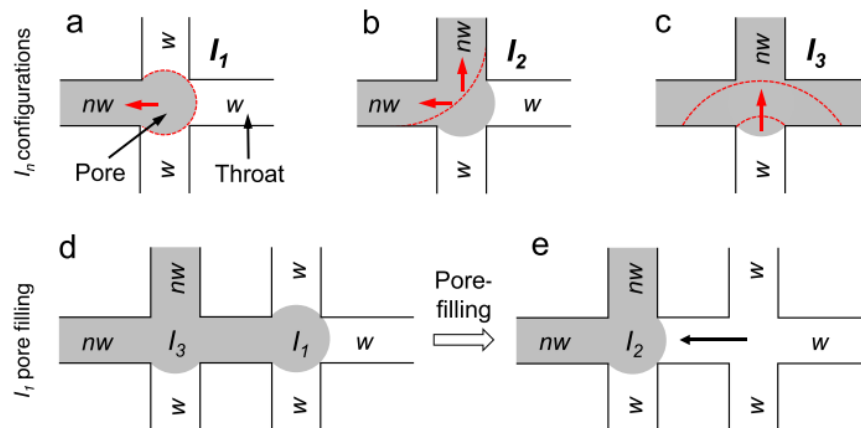


Figure 6: Diagrammatic representation of cooperative pore filling imbibition events⁹.

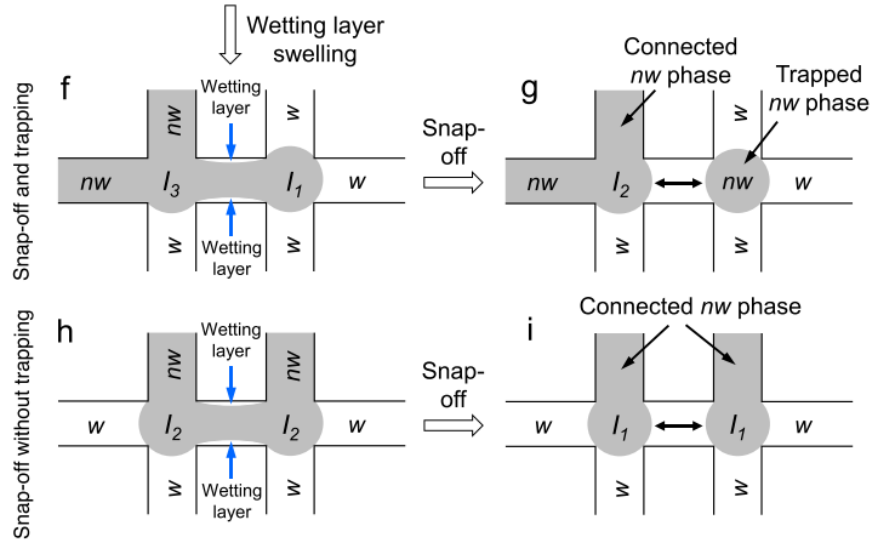


Figure 7: Diagrammatic representation of two snap-off events, one of which results in trapping⁹.

After drainage, not all of the wetting fluid will have been displaced from the pore space. In corners and along the roughness of grain surfaces²⁵, wetting fluid remains as thin films. Wetting fluid also remains in small pores that the non-wetting fluid could not enter. As imbibition occurs, the wetting fluid films begin to swell. When these films swell in pore throats and films from the opposite side of the throat wall touch, the fluid/fluid interface becomes unstable and the throat suddenly fills with wetting fluid^{9,32}. This is called snap-off. It only occurs if no pore adjacent to the throat is filled with wetting fluid, as a piston-like displacement would occur instead if that were the case³⁰. Snap-off typically occurs when the aspect ratio (ratio between pore radius and throat radius) is high. This type of event causes the connection between the non-wetting fluid in the pores on either side of the throat to be broken as shown in Figure 7. As a result, the topology (connectivity) of the system changes. Cooperative events of type l_2 or higher also change the connectivity of the system. This may lead to trapping of the non-wetting phase⁹.

Trapping

Trapping is directly linked to the connectivity of fluids. It contributes strongly to multi-phase flow hysteresis³³, which will be explained in a later section. Trapping results in residual saturation of a fluid. This residual saturation consists of subregions of non-wetting fluid that have become disconnected from the connected bulk non-wetting fluid. They are completely surrounded by wetting fluid and are thus hydraulically isolated within the pore space (see Figure 8)³³. This phenomenon can for example be used to safely store CO₂ during geological carbon dioxide sequestration.

Trapping occurs primarily during imbibition. It is mostly the result of snap-off, but co-operative pore filling can also lead to trapping, albeit on a less frequent basis¹⁹. Trapping can also occur as a result of bypassing, where the wetting fluid advances as a front but sections of it join ahead of other sections, disconnecting larger clusters of non-wetting fluid from the connected non-wetting fluid.

Well-connected pore spaces typically exhibit less trapping, because the non-wetting fluid has more possible escape paths. Strongly-wetted systems (systems where the contact angle is either close to 0° or 180°) encourage layer flow, which causes more snap-off. This means strongly-wetted systems exhibit more trapping. Higher co-ordination numbers also mean trapping occurs less, as the non-wetting fluid has more pore throats through which it can escape. The aspect ratio also influences trapping, as higher aspect ratios encourage snap-off, which causes more trapping¹⁹.

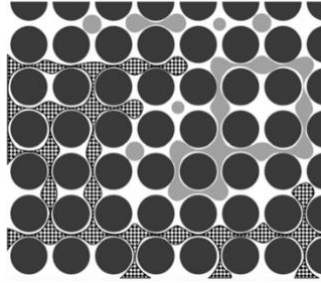


Figure 8: Conceptual image of trapped non-wetting fluid (light grey) surrounded by wetting fluid (white). The check-patterned fluid is connected non-wetting fluid (image adapted from Joekar-Niasar et al.³³).

Relative permeability

Continuum scale properties such as relative permeability are needed to make large-scale models to characterize transport during for instance CO₂ sequestration, oil recovery, etc³⁴. Permeability is an intrinsic property of the pore space, depending on the pore structure of the system. It gives an indication of the level of ease with which a fluid can flow through a porous medium and it is measured when the pore space is occupied by a single fluid. In multiphase flow, the pore space is filled with more than one fluid. This means that each fluid cannot flow through the entire pore space, as portions of the pore space are already occupied by the other fluid(s). The effective permeability of each fluid is therefore lower than the intrinsic permeability. Relative permeability is a value between 0 and 1, describing this decrease in effective permeability as a function of the saturation of the fluid¹⁹. Saturation here refers to the proportion of pore space which is occupied by the fluid, expressed as a value between 0 and 1, where 0 means there is none of that fluid present and 1 means that the entire pore space is filled with that fluid. As the saturation of a fluid increases, so does its relative permeability and vice versa as seen in Figure 9. Relative permeability is determined through expensive, time-consuming experiments which deploy either steady state or non-steady state methods²⁹. Since the wettability of a system determines how fluid displacements occur and therefore how fluids flow, the relative permeability is heavily affected by the wettability. The importance of these continuum scale properties motivates their determination by pore-scale modelling, based on pore-scale properties such as wettability, pore space geometry, etc.

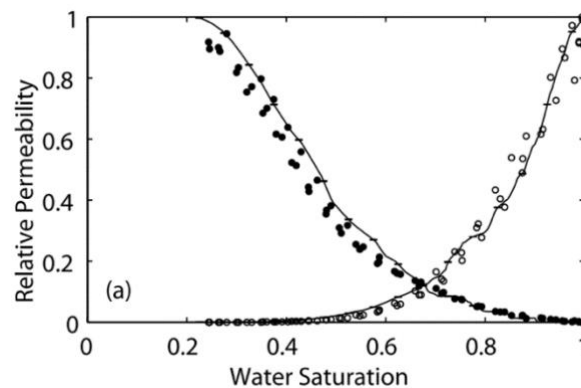


Figure 9: Above is a graph showing the relative permeability curves during drainage for an experiment. The filled in circles show the relative permeability of the non-wetting fluid, while the empty circles show the relative permeability of the wetting fluid³⁰.

2.1.2. Hysteresis in multiphase flow

Hysteresis is a process which refers to path dependence, or irreversibility. In multiphase flow, this is manifested by the capillary pressure and relative permeability functions which depend on the saturation history²⁵. In capillary pressure graphs, the imbibition curve is always below the drainage curve, indicating at a given saturation, imbibition occurs at lower capillary pressures. The imbibition curve lying below the drainage curve is explained by the ink bottle effect³⁵, because drainage is mainly controlled by the size of the narrowest passages (throats) through which the fluid/fluid interface must travel and imbibition is rather controlled by the largest passages (pores) through which the fluid/fluid interface must travel. The narrower pore throats correspond to a higher threshold capillary pressure than the wider pores, explaining why drainage occurs at higher capillary pressures than imbibition. Primary drainage capillary pressure curves start at a wetting-fluid saturation of 1, since at the start of the experiment the entire pore space is filled with wetting fluid, and then capillary pressure increases as wetting saturation decreases as seen in the right figure of Figure 10. Subsequent imbibition curves never reach a wetting saturation of 1 again, due to trapping¹⁹.

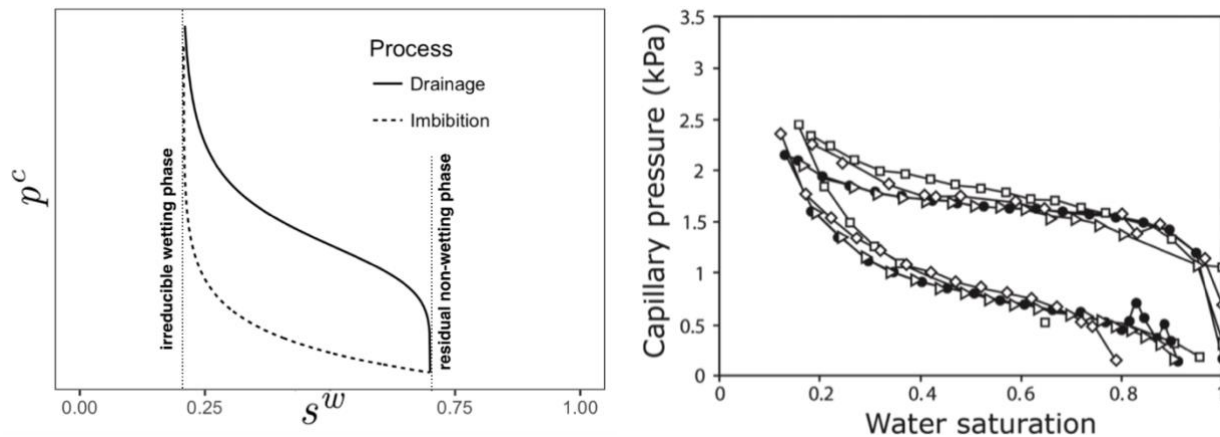


Figure 10: Capillary pressure curves, illustrating capillary pressure hysteresis. The left shows a theoretical curve illustrating the typical shape of imbibition and drainage curves³⁵. s^w indicates wetting-fluid saturation and P^c indicates capillary pressure. The right shows an experimentally obtained primary drainage curve (hence the wetting-fluid saturation of 1 can be seen as part of the top curve) and a secondary imbibition curve which is the bottom curve (figure taken from Blunt¹⁹, adapted from Plug & Bruning³⁶).

Relative permeability hysteresis, as with capillary pressure, is very clearly visible along the saturation axis, as during imbibition, saturations as high as those seen during drainage are not encountered again (Figure 11). This can be explained by trapping. The cross-over point of the wetting and non-wetting relative permeability curves also shifts when comparing imbibition to drainage. Other causes of capillary pressure and relative permeability hysteresis include contact angle hysteresis^{25,37,38}, complexity of the topology and geometry of the interconnected pore space³³ and geological heterogeneity³⁸. Researchers have attempted to create empirical models to capture this hysteresis from as early as 1968³⁹. These models have focused on characterising relative permeabilities as well as trapped saturation of the non-wetting fluid once drainage and imbibition have finished^{37,39-44}.

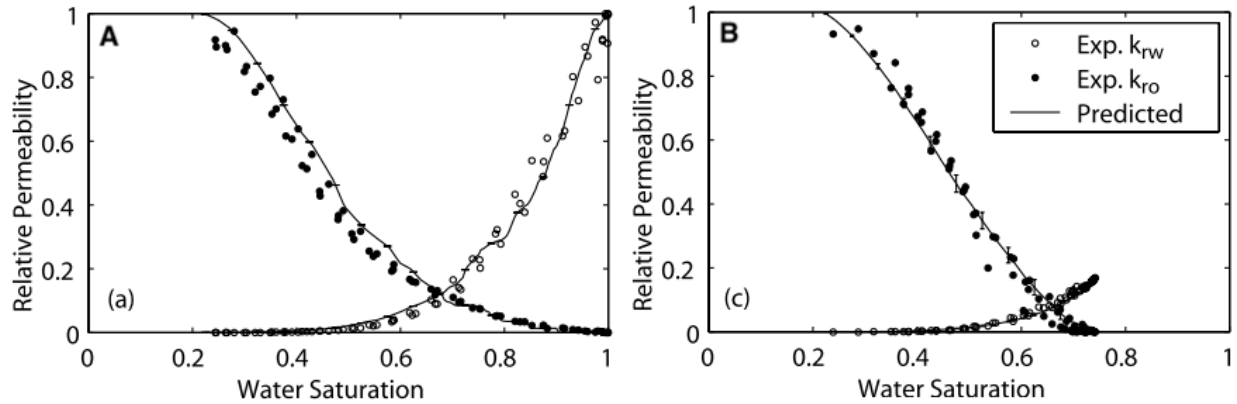


Figure 11: A shows the relative permeability curves during drainage for an experiment. B shows the relative permeability curves during imbibition for an experiment. The filled in circles show the relative permeability of the non-wetting fluid, while the empty circles show the relative permeability of the wetting fluid. Hysteresis is especially visible towards the right of curves, where the imbibition saturations remain below 0.8, while the drainage saturations reach 1³⁰.

2.1.3. Contact angle hysteresis

Contact angle hysteresis is one of the sources of hysteresis seen in capillary pressure curves and relative permeability^{25,37,38}. The two most prominent causes of contact angle hysteresis in nature are wettability alteration and surface roughness. Wettability alteration occurs when surface-active compounds (such as certain petroleum components) sorb to the solid surfaces in a porous medium. This changes the interfacial tensions between the solid and the fluids, hence changing the contact angle¹⁹.

Surface roughness does not change the intrinsic contact angle that the fluid meniscus makes with the solid surface. It does however influence the effective contact angle, which is the angle measured as if the surface were smooth (Figure 12). This effective contact angle is what determines the curvature and hence, controls displacement. The effective contact angle depends on the direction of fluid displacement, resulting in contact angle hysteresis¹⁹. The fluid/fluid contact line can become pinned by surface roughness. If one thinks of roughness as a series of 'edges', each edge can make the contact angle flexible at that point (Figure 13). Before the edge, we measure a contact angle of θ , and immediately after the edge we measure a contact angle of $180^\circ - \Phi + \theta$ (using the horizontal as a reference and ignoring the existence of the edge with the naked eye). This means at the edge, any contact angle between θ and $180^\circ - \Phi + \theta$ can occur. This makes contact angles dependent on the history of the flow path. Relating what happens on the nano-scale to macroscopic observations is challenging as the larger-scale observations of hysteresis are based on the averages of the effects of many of these 'edges'²⁰.

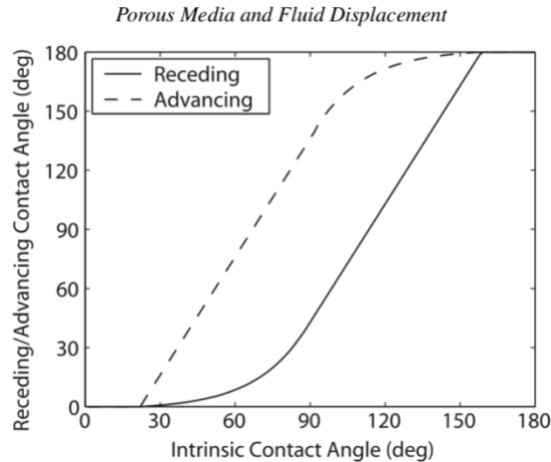


Figure 12: Diagram showing the relationship between the advancing and receding contact angles on a rough surface, based on the intrinsic contact angle. Figure taken from Valvatne & Blunt³⁰, adapted from Morrow⁴⁵.

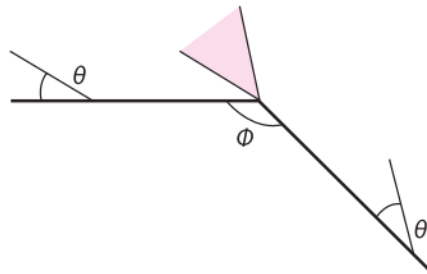


Figure 13: A diagram showing the apparent pinning of a contact angle on an edge. The Young condition states that the contact angle must be θ , hence at the edge any angle between θ and $180^\circ - \phi + \theta$ can occur, as illustrated by the coloured portion of the figure²⁰.

Other possible sources of contact angle hysteresis are chemical heterogeneity within the pore space. Flow rate can also introduce contact angle hysteresis, but at the slow flow rates encountered in most systems of interest to this project, this is assumed to play an insignificant role¹⁹.

2.2. State-of-the-art

2.2.1. Fluid displacement in two-dimensional systems

Through the years, there have been relatively few experimental studies on pore-scale displacement patterns and wettability properties during multiphase fluid flow³². Until recently, observations of dynamic events at the pore-scale during multiphase flow could only be achieved by using 2D porous media that can be imaged by optical methods^{32,46}. Some of the first of these were pioneering experiments performed by Lenormand and co-workers. They involved using 2D micro-models to observe pore-scale events⁴⁷⁻⁴⁹. These early experiments looked at the extreme cases of fully wetting or fully non-wetting invading fluids and made use of square lattices composed of capillary ducts. Shortly after, Cieplak and Robbins^{50,51} as well as Martys et al.⁵² constructed numerical simulations to model the 2D fluid interfaces in pore scale multiphase flow, by using contact angles and contact angles coupled with pressures as the main input variables respectively. Further experimental work made use of wettable disk arrays to probe the pore-scale fluid distributions during multiphase flow. One such model porous material was created by Chraïbi et al.⁵³ which made use of homogenous wettable disk arrays to study the influence of contact angles on evaporation in 2D models³². The evaporating liquid was treated as a wetting gas which was replaced by a

non-wetting gas, hence the drying process could be viewed as drainage. More recent experiments by Zhao et al.¹⁰ (Figure 14) explore how the displacement patterns depend on a nearly continuously varied advancing contact angle. In this work, high resolution optical imaging is used in conjunction with microfluidic flow cells consisting of vertical posts. The wettability of the flow cells is systematically changed (by illumination with UV-light) in order to study the effect this has on how fluids flow through the medium. This study found wetting layer flow to be a significant displacement mechanism, which the Cieplak-Robbins model fails to capture. The Cieplak-Robbins model also fails to capture the snap-off instability, which is essential for models of multiphase flow in natural porous media³². These studies made use of well-controlled samples which are easily visualized at high spatial and temporal resolutions. Their drawback is that they fail to capture the complexity of natural media. These types of experiments were thus a precursor to the experiments by which the data used in this dissertation was obtained.

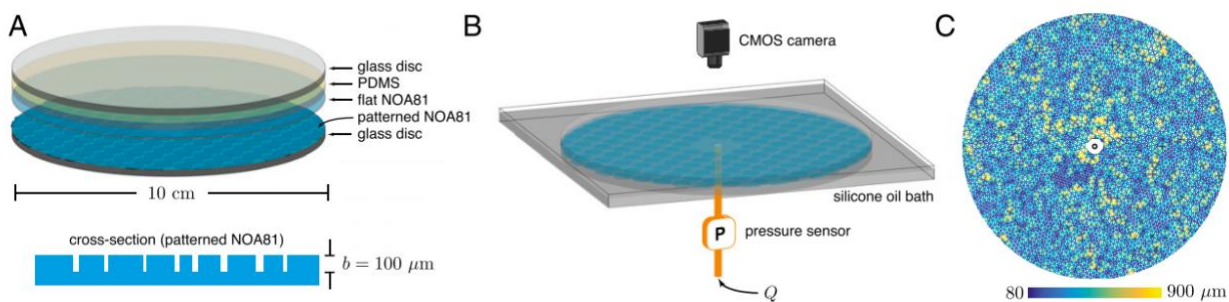


Figure 14: Schematic of a quasi-2D microfluidic flow cell. B shows how the experiment is imaged using a camera and C shows the pore size distribution of the flow cell¹⁰.

2.2.2. Three-dimensional imaging of fluid flow

In the previous decade, 3D imaging techniques have become widely available. These techniques provide valuable insight into 3D structures and dynamics, but have several limitations. Confocal microscopy, while being a fast imaging technique, brings with it several limitations that were also seen in the 2D micro-models³²: it requires optically transparent micro-models and is hence limited to thin glass bead packs. It also requires the refractive indices of the wetting fluid, non-wetting fluid and glass beads to be matched⁵⁴. Tomographic imaging techniques such as X-ray CT and neutron CT are techniques which have been well established to characterise the internal 3D structure of porous media or to observe static fluid distributions in them^{55,56}. With its recent advances, dynamic X-ray CT provides in many cases a good compromise between temporal and spatial resolution (on the order of micrometers and seconds, respectively), often making it an excellent imaging method for dynamic pore-scale multiphase fluid flow experiments³².

X-ray μ CT, which will be discussed in detail in Section 3.1, has not only allowed for the study of fluid distributions in the pore space of rocks, but also for the study of more detailed properties of the fluid menisci. The first curvature-based capillary pressure estimation was conducted in a study by Armstrong et al.⁵⁷, where interfacial curvature measurements were used in conjunction with the Young Laplace equation (Eq. 4). The aim of this study was to investigate how capillary pressure evolved during drainage and imbibition experiments. This was the first study to experimentally compare pore-scale capillary pressure measured via interfacial curvature to macro-scale capillary pressure measured using an external pressure transducer. The same method was used in this dissertation.

A new form of wettability determination in porous media was introduced in a study conducted by Andrew et al.⁵⁸, which was the first study to measure geometric contact angles of fluid distributions inside of porous rock by using μ CT images. Before this, contact angle measurements could only be made macroscopically

or in micromodel studies (as described above). The drawbacks to the former of these are that they are made on smoother, less complex surfaces that do not account for the roughness and heterogeneity seen in the pore space. The fluid flow experiments in this study⁵⁸ were carried out on a Ketton Limestone sample. Within the 3D volume obtained by the μ CT imaging, the three-phase-contact-line was identified around a few chosen trapped CO₂ ganglia. 300 contact angle measurements were made by randomly selecting points on the three-phase-contact-line, identifying the plane perpendicular to that line at that point and measuring the angle between the fluid/fluid interface and the brine/solid surface. The method produced a contact angle distribution of over 30° (Figure 15). This wide distribution is partly due to the measurements being made on static fluid distributions.

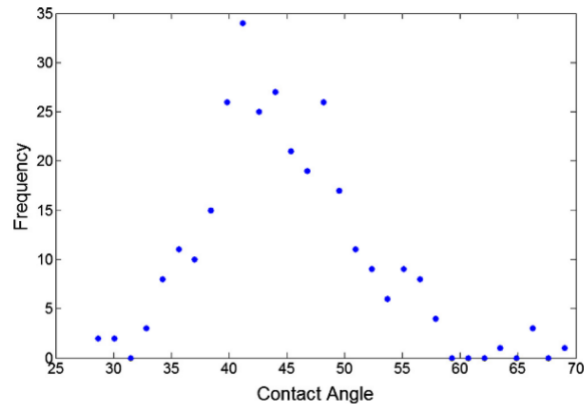


Figure 15: Distribution of manual geometric contact angles measured by Andrew et al.⁵⁸ on a Ketton limestone μ CT dataset.

The method of manual contact angle measurements has been applied on glass bead and sand packs to investigate the effects of ionic strength, phase state and flow path^{59,60} and on micromodels to assess dynamic and static contact angles⁶¹. It has also been applied on sandstones to measure contact angles of static fluid distributions at reservoir conditions¹² and to compare different contact angle measuring tools⁶² and methods⁶³; and on carbonates to investigate the effect of wettability on oil entrapment and oil layer formation⁶⁴. It has been used in many other studies as a form of validation for other geometric contact angle determination methods^{13,65,66} (as in this dissertation). All of these measurements (with the exception of some of those made by Jafari and Jung⁶¹) were made on static fluid distributions within the pore space.

The approach of manual contact angle measurements developed by Andrew et al.⁵⁸ is time consuming and may be prone to subjectivity. This led to the development of automated methods of geometric contact angle measurements. The first of these was an algorithm developed by Klise et al.⁶⁷ which determined local contact angle measurements by fitting planes to both the fluid/fluid interface and the fluid/solid surfaces⁶⁸. This method was later used by Dalton et al.⁶² on sandstone cores to compare automated contact angle measurements to older methods of contact angle determination (sessile drop).

A different automated algorithm, developed by Scanziani et al.⁶⁵ was based on the manual measurement method of Andrew et al.⁵⁸. It uses the insight that the fluid/fluid interface has a constant curvature by the Young Laplace law. This algorithm yields the angle that the fluid/fluid interface would have if the surface was locally smooth. The output of this method is therefore the effective contact angle. This is the value which would be used in pore-scale models as it is said to incorporate roughness, local pore geometry as well as flow direction. Scanziani et al.⁶⁵ tested the algorithm on two experimental datasets obtained from μ CT imaging of drainage and imbibition experiments on Ketton limestone samples. They compared the results to the method of manual geometric contact angle measurement and found them to be in good agreement. In the algorithm, the contact angle is computed as the angle between the tangent to a circle

fitted to the fluid/fluid interface curvature at the three-phase-contact-point and the rock-surface line. This method generates thousands of estimations of contact angles, allowing the measurements to be analysed in a probabilistic framework. In the original study⁶⁵, calculations were done on tomographic images taken after water-flooding was complete, so the fluid distributions were at rest. This method was also used in a study to determine static contact angles between oil and brine in a carbonate sample where three-phase flow was being investigated⁶⁹.

Another automated algorithm for in situ contact angle measurements was developed by AlRatrouf et al.¹³. This algorithm applies a variety of smoothing operations to voxelized pore-scale images and then calculates the vectors perpendicular to the fluid/fluid interface and fluid/solid surfaces. The contact angle is then calculated by taking the dot product of those two vectors where they meet at the three-phase-contact-line. This approach also uses the insight of a constant fluid/fluid interfacial curvature. The wettability of calcite cores at reservoir conditions was investigated using this method⁶⁶. It was also used on carbonate samples from a producing hydrocarbon reservoir to study the correlation between contact angle and interfacial curvature⁷⁰. Another study investigating the relationship between surface roughness and wettability also used this method to determine contact angles in a limestone sample⁷¹. This algorithm developed by AlRatrouf et al.¹³ was the method of geometric contact angle determination used in this dissertation.

It falls into question how relevant measurements from the studies mentioned above are, since measurements were made on fluid distributions that were at equilibrium (or near equilibrium). This is because the contact angles (or curvatures) measured using these methods are at rest and as such have come to an equilibrium at a value somewhere between the advancing and receding contact angles (and corresponding curvatures)⁵⁸. If we want to use these measurements in pore-scale models to make predictions of continuum-scale properties (such as relative permeability), we need contact angles that are linked to the fluid displacement. This means we need measurements that take the dynamic nature of fluid displacements into account, not measurements made on static fluid distributions.

Recently, Mascini et al.¹⁴ developed a technique to measure contact angles which does take the dynamic nature of fluid displacements into account. Event-based contact angles use measurements in pores of the event and pores surrounding the event in the timestep preceding the event. This means that contact angles measured are not at rest and instead are closer to the advancing contact angle (for imbibition) or the receding contact angle (for drainage). It is these contact angles that determine the fluid dynamics. These are the contact angles that should be quantified for use in pore-scale models if we hope to accurately predict continuum-scale properties. The remaining limitation is the resolution of the imaging data. Displacement events are typically fast occurring, with some occurring on a millisecond timescale which is equivalent to the time required to take a single radiograph⁷². Ideally, we would want measurements taken immediately prior to these events. μ CT is not capable of this level of temporal resolution currently, even at synchrotrons (which are capable of 1 s/scan¹⁴). As the technology continues to improve, so will the accuracy of this type of measurement.

2.2.3. Time-resolved fluid flow in three-dimensional systems

The non-destructive nature of μ CT means that it is capable of imaging dynamic processes that occur within a medium by taking tomographic images of the sample at various points in time. For more detail on the method of X-ray CT, refer to section 3.1. In order to use these images to perform quantitative analyses, they must be perfectly aligned. This means that for this type of experiment to work, the sample should not be moved in between imaging steps⁷³. It is also possible to fit various equipment with fluid flow lines in the workspace of some μ CT scanners. A constraint is that to achieve high quality images, the fluid flow processes must be slower than the image acquisition times, or the fluid distribution must be stable at the

time of imaging. In order to obtain a good signal-to-noise ratio, exposure times must be long enough, resulting in a trade-off between temporal resolution and image quality⁷⁴. The emergence of this type of experiment has encouraged the development of specialized sample containers, which are ideally cylindrical in shape, small in size (one to a few cm in diameter) and are made up of materials that are transparent to X-rays while still being mechanically robust (such as aluminium or carbon)⁷³.

Pseudo real-time visualizations of dynamic processes occurring within a sample are possible using continuous imaging. This is the type of data that was used in this dissertation. This method allows for the viewing of how the sample evolves over time and is well suited to fluid flow experiments. Time-lapse CT, on the other hand, is well suited to slow processes where the sample only needs to be imaged at set times. Time-lapse CT has been performed at both synchrotron facilities as well as laboratory μ CT setups. Over the previous couple of years, dynamic, continuous experiments have started being undertaken at synchrotron facilities. These experiments now being possible, is due to the emergence of fast read-out detector technology as well as fast computer memory. This allows researchers to make use of the high flux generated at synchrotron beam lines to shorten image acquisition times to the order of seconds in some cases. This in turn allows for the capturing of fast processes without image blurring⁷³. Some studies on multiphase fluid flow dynamics have been conducted at synchrotrons. Experiments include imaging of Haines jumps in sandstones⁷², imaging of remobilization of the trapped non-wetting phase⁷⁵ and imaging of ganglion dynamics⁷⁶, to list but a few.

2.3. Contact angle measurements

2.3.1. Geometric contact angles

In the past, viewing the contact angles in porous media was only possible in micromodels^{58,77}. The advance of μ CT has allowed for contact angles to be measured inside porous geological material by conducting geometrical analyses on 3D images taken of these systems¹⁴. The geometric contact angle is the angle which the fluid/fluid interface makes with the solid surface, measured from a point on the three-phase-contact-line, in the plane perpendicular to this line at that point (see Figure 16)⁵⁸. The three-phase-contact-line is the line where the wetting fluid, non-wetting fluid and solid surface meet. These measurements can be made by using visual observations⁵⁸, automated algorithms¹³ or by using methods utilising the deficit curvature of the interfaces^{14,18}.

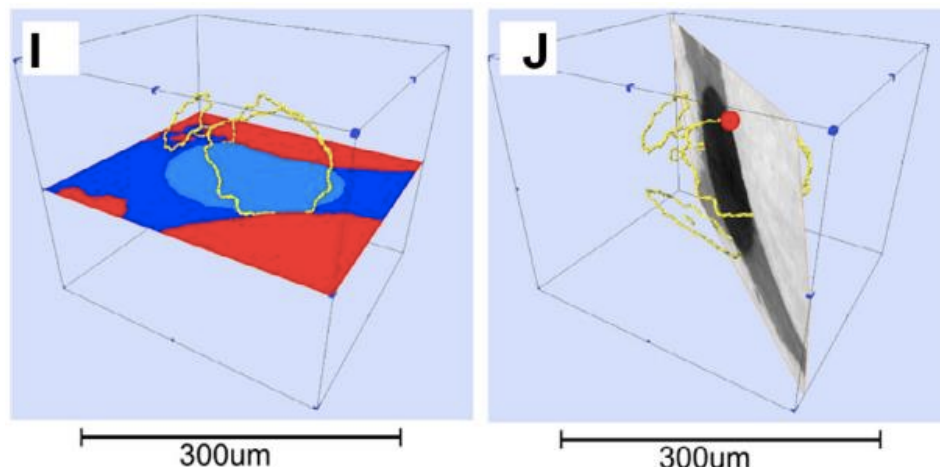


Figure 16: I shows a cross section where red is the grain, dark blue is the wetting fluid and light blue is the non-wetting fluid. The yellow line is the three-phase-contact-line. In J, the cross section now corresponds to the plane perpendicular to the three-phase-contact-line at the red dot. It is on this plane that the contact angle is measured⁵⁸.

2.3.2. Force-based contact angles

Geometric contact angle measurements are highly affected by both the image resolution as well as surface roughness. To lessen these effects, Mascini et al.¹⁴ developed the force-based contact angle, which makes use of the curvature of the fluid/fluid interface rather than the angle between this interface and the solid. This means that measurements are used which are further away from the grain boundaries and as such are not as impacted by surface roughness. Since the curvature information is gathered from a larger region of the 3D image, it is less impacted by the resolution than the geometric contact angle would be. The interfacial curvatures are mapped to the pores in which they occur. In the timestep preceding an event, the fluid/fluid interface is located partly in the pores of the event and partly in the pores neighbouring the event. The capillary pressure is therefore determined by calculating the average curvatures in the pores of the event as well as the pores neighbouring the event one timestep prior to the event occurring, by using Eq. 4. This then also relates to the force-based contact angle by Eq. 4, which can be further adjusted to give:

$$\theta_f = \cos^{-1}(k_{thr}r) \quad \text{Eq. 5}$$

where θ_f is the force-based contact angle, k_{thr} is the threshold curvature and r is the throat radius, if the experiment is of drainage, or the pore radius if the experiment is of imbibition. It is important to note that in this equation, θ_f only yields the same value as the actual contact angle if the pore/throat is cylindrical¹⁴.

2.3.3. Thermodynamic contact angles

Blunt et al.¹⁵ developed a method for estimating the contact angle (called the thermodynamic contact angle) which reduces the impact of image quality as well as the impact of the equilibration times before an image is taken^{14,15}. Geometric contact angles are measured on images taken when the fluid/fluid interfaces are at rest. Pore-scale displacements occur at the micro- to milli-second scale and as such, even the fastest μ CT imaging cannot capture these exact events^{15,19}. The thermodynamic contact angle is based on energy conservation. This method estimates the system's stored interfacial energy as the pressure-volume work. Tomographic images are taken before the start of imbibition and are then compared to tomographic images taken at the end of imbibition. The pressure-work is then estimated by measuring the change in saturation as well as the curvature of the fluid/fluid interface. The stored interfacial energy can be expressed as a function of the thermodynamic contact angle and interfacial areas^{14,15}. The thermodynamic contact angle is an effective value as it represents the angle corresponding to the observed change in interfacial energy which is caused by displacements. It does not represent the contact angle which is measured directly from μ CT images at the micro-scale¹⁵. It assigns the entire sample a single value, giving no localized measurements¹⁴. Mascini et al.¹⁴ extends the work of Blunt et al.¹⁵ to reach the equation for thermodynamic contact angle in the case where fluid 1 is displacing fluid 2:

$$\cos \theta_t = \frac{2k_{thr}\Delta V_1 + \Delta A_{1,2}}{\Delta A_{1,s}} \quad \text{Eq. 6}$$

where θ_t is the thermodynamic contact angle, k_{thr} is the threshold curvature, ΔV_1 is the change in volume for fluid 1 (it should be positive since fluid 1 is displacing fluid 2), $\Delta A_{1,2}$ is the change in the interfacial area of the fluid/fluid interface and $\Delta A_{1,s}$ is the change in the fluid 1 – solid surface area.

2.3.4. Event-based contact angles

In many studies, contact angles are measured based on μ CT images taken where the fluid/fluid interface remains static. Information is lost since the dynamics of displacement events are not taken into account. Event-based contact angles were introduced by Mascini et al.¹⁴ to solve this problem. Time-resolved μ CT images are used to identify displacement events and measure the contact angles in pores in and adjacent to the events one timestep before the event occurs. An event is identified when a pore's occupancy changes (see Figure 17). Connected fluid fillings occurring in the same timestep are grouped into the same event¹⁴.

Geometric contact angles, force-based contact angles and thermodynamic contact angles can be measured this way, yielding event-based measurements.

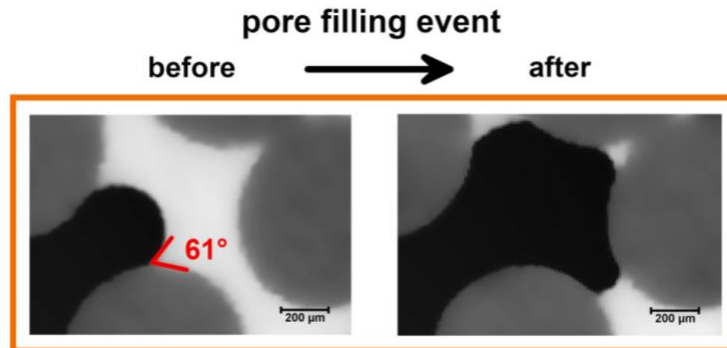


Figure 17: An image of a pore filling event during drainage. The left shows the image just before the event occurs. The pore is filled with wetting fluid. The right shows the image just after the event occurs. The pore is now filled with non-wetting fluid, hence its occupancy has changed¹⁴.

3. Materials and methods

In the following section, the X-ray CT imaging method will be explained. A dynamic μ CT dataset was used in this dissertation, making an introduction to the method necessary as the method has an important effect on the artefacts of the dataset. This in turn affects how the analyses were conducted. After this, the dataset will be discussed, followed by a sensitivity analysis of image processing and a description of the various aspects of the image analysis.

3.1. X-ray CT

3.1.1. Basic principles

X-rays are electromagnetic radiation with high energies and experience differential attenuation when interacting with different materials. It is this property that makes them useful for imaging⁷⁸. X-ray CT is able to provide structural information of geomaterials on a scale ranging from sub-micron to millimetre. This makes it useful for multiscale characterisation. The technique is based on the Lambert-Beer Law (Eq. 7), which describes the attenuation of X-rays as they pass through and interact with materials. X-ray radiation is able to penetrate different materials by varying degrees, which is a useful characteristic⁷⁴.

$$I = I_0 e^{-\int \mu(s) ds} \quad \text{Eq. 7}$$

The intensity of the transmitted X-ray (I) depends on the initial intensity (I_0) as well as on the linear attenuation coefficient (μ) and the raypath (s). The linear attenuation coefficient in turn, depends on the density of the materials as well as on its atomic number. Since multiple parameters affect the transmitted X-ray intensity, directly identifying the chemical makeup of the material by X-ray CT is difficult⁷³. The Lambert-Beer Law is only valid for monochromatic X-rays which follow a linear path. In μ CT, these conditions are not always met, resulting in reconstruction artefacts⁷⁴ which will be discussed later.

From Eq. 7 it is clear that the integrated μ can be calculated for every point on a radiograph. In CT, the sample undergoes rotational movement relative to the X-ray source and detector, producing many radiographs ('projection images') over a wide angular range. By using reconstruction algorithms, the μ at every point in the scanned 3D volume can be determined⁷⁴.

3.1.2. X-ray systems

Source

An X-ray CT setup consists of both a source which produces the X-rays as well as a detector, which measures the transmitted X-rays. X-rays are produced at the source when the kinetic energy that electrons obtain when accelerated is converted to electromagnetic radiation. This occurs when the momentum of the electrons changes⁷⁸. In laboratory setups, this momentum change comes from collisions of electrons with a target material, producing bremsstrahlung X-rays⁷⁹. At a synchrotron, however, change in momentum comes from maintaining the circular motion of electrons in storage rings. The X-rays are emitted tangentially to the path of the electrons, in a very narrow cone. The electrons are kept on their circular paths by using bending magnets. They can also be accelerated by wigglers and undulators to obtain more brilliant X-ray beams. Here, the electrons are run through a series of dipole magnets, which amplifies the intensity of the radiation⁸⁰.

Detector

The detector is usually a 2D pixel array, such as a CCD camera, flat panel detector or image intensifier. The detector is responsible for converting the X-rays to a digital radiograph⁸¹. Indirect detectors are most commonly used, where the detector is made up of a scintillator which converts X-rays to visible light (see Figure 18) and a photodiode which converts this visible light to an electric current so that the image can be stored digitally⁷⁹. Direct detectors measure incoming X-ray photons directly. While this method has potential for higher resolutions, since it discards the need for scintillators which introduce resolution constraints, it is still under development.

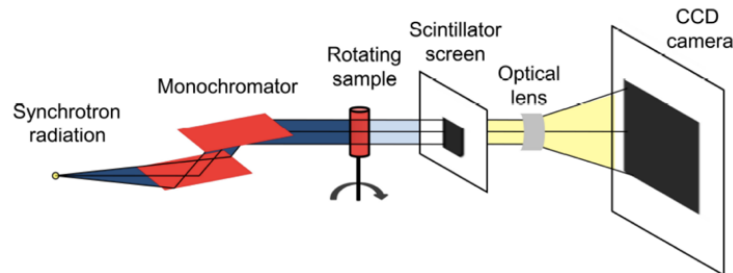


Figure 18: Schematic showing how imaging at a synchrotron occurs. The scintillator screen converts X-rays to visible light. The parallel nature of the X-ray beam means geometric magnification is not possible without the use of optics⁷⁴.

Synchrotron μ CT

In most lab-based and in synchrotron μ CT setups, the source and detector remain stationary while the sample rotates in between the two (see Figure 18). This ensures higher levels of mechanical stability which are needed to achieve higher resolutions⁷⁴. A radiograph is recorded at the detector. The intensity of the X-rays which reach the detector depend on the thickness, the density and the chemical composition (atomic number) of the sample⁷³. The cone beam used in laboratory-based μ CT means magnification is possible by moving the sample closer to the source, though this results in a smaller field of view. The X-ray beam produced by synchrotron sources is almost parallel (see Figure 18). This makes geometrical magnification impossible without the use of X-ray optics. At synchrotrons, thin scintillators can be used, due to the high flux. Lab-based CT requires the use of thicker scintillators due to the relatively low X-ray flux. This increases the sensitivity to X-rays, but results in a lower maximum obtainable resolution⁸⁰.

Over an angular range of 360° (or 180°), hundreds to thousands of radiographs are recorded and then combined into a 3D volume using reconstruction algorithms⁸². The most common reconstruction method is

filtered back-projection. The attenuation profile is first run through a filtering function before back-projection is done. The filtered projection contains some negative values that precisely cancel out star-burst patterns when back-projection is then performed. This results in an image which is an accurate depiction of the original sample⁷⁹ (see Figure 19).

The 3D volume shows the distribution of linear attenuation coefficients, depicted using grey scale values, and is stored as a stack of 2D slices. High resolution images can be acquired by laboratory μ CT with a time frame of several minutes to hours. At synchrotrons, high resolution images can be acquired in seconds to a minute. This is thanks to the high X-ray flux generated by synchrotron beam lines⁷³.

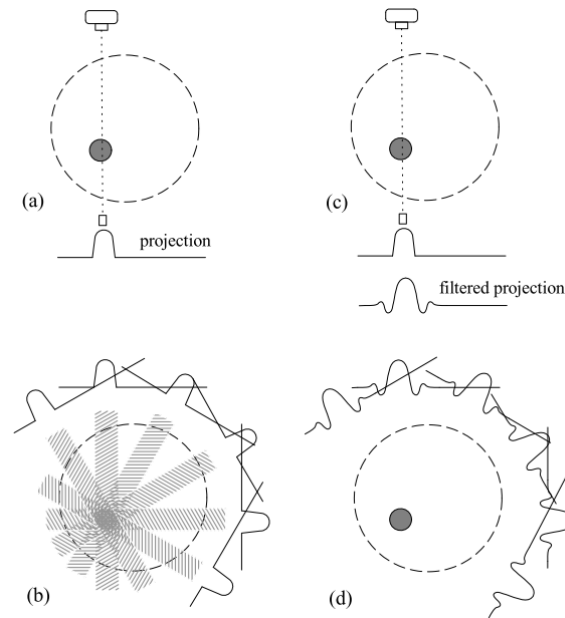


Figure 19: a) and b) show simple back-projection, resulting in a star-burst pattern. c) and d) show filtered back-projection, resulting in an accurate representation of the original sample⁷⁹.

3.1.3. Image quality and artefacts

Resolution

The resolution of the tomographic images depends on the geometrical magnification, the focal spot size, the pixel size of the detector and on various physical phenomenon (such as X-ray scattering). The magnification (M) is defined as the ratio of the distance between the source and the detector over the distance between the source and the sample. This means that the closer the sample is to the source, the more magnified the image is. Due to the conical nature of the incident X-ray beam, the closer the sample is to the source, the smaller the investigated volume becomes, in laboratory-based setups. This means that at a certain proximity, the field of view will be smaller than the size of the sample and not all of the sample will be imaged by the X-ray beam. This is the sample size-resolution trade-off. The focal spot is the area of interaction of electrons and hence the area from which X-rays are emanated from the source. Smaller focal spots can result in higher spatial resolutions but they impose challenges, such as overheating and lower X-ray flux⁷⁸, resulting in lower temporal resolutions⁷⁴.

As with all imaging techniques, μ CT experiences noise. The lower limit of this noise is determined by the number of photons detected and is equivalent to the Poisson noise. Image noise, in practise, is generated by several parameters, especially when scintillators are involved. The lower limit of electronic noise is

theoretically obtainable by making use of photon counting detectors (direct detectors)⁷⁴. The counting statistics depend on the total number of photons measured, however. Since direct detectors can handle a lower flux than indirect detectors can, this means they are much slower.

Discretization and partial volume effects

Discretization effects influence image quality. Projection images are always captured using a 1D or 2D detector. After reconstruction, a 3D volume made up of voxels (volume elements) is generated. This discretization impacts image quality by controlling the lowest possible voxel size. The rotational movement of the sample results in the volume that is imaged being cylindrical⁷⁴. The imaged volume is divided into N_d number of pixels which are perpendicular to the axis of rotation of the sample. This results in the minimum distance between the centres of adjacent voxels (v_d) in the reconstructed volume being⁷⁴:

$$v_d = \frac{D}{N_d} \quad \text{Eq. 8}$$

For computational reasons, the number of pixels (N_d) is limited, which means the minimum possible voxel size depends on the diameter (D) of the imaged cylinder. In order to minimize artefacts, the size of the sample used is selected so as to closely match the imaged volume. This means the minimum voxel size achievable is linked to the sample size⁷⁴.

Any features smaller than the voxel size cannot be resolved in the tomographic image. They do still affect the image, however, due to the 'partial volume effect'. The reconstructed value of a voxel is the average linear attenuation coefficient over the entire volume of that voxel. This effect also occurs in voxels encompassing edges of structures. The voxel containing an edge takes on a grey value intermediate to the two (or more) phases within the volume of the voxel. This causes the edges of structures in μ CT images to appear blurry. This 'partial volume effect' can be used to calculate porosity in each voxel when pores are smaller than the resolution, by deploying differential imaging techniques⁸³. Usually, however, this effect is seen as an image artefact which reduces the accuracy of the analysis⁷⁴.

Artefacts

As seen above, Eq. 7 is only valid for monochromatic X-rays. At laboratory setups, polychromatic X-rays are used, resulting in an artefact called 'beam hardening'. At synchrotrons, monochromatic X-rays are used, so this artefact is not present⁷⁴.

The conical nature of the X-ray beam in laboratory μ CT is another source of artefacts. Slices far from the centre of the imaging volume can accrue extreme artefacts due to this 'cone beam effect'. This effect poses a particular problem when studying object surfaces or layered samples. The effects are greater when the angle of the cone beam is larger. Its effects can be diminished by applying iterative reconstruction methods or by employing a helical scanning trajectory⁷⁴. Again, this artefact does not occur when using a synchrotron X-ray source.

Another serious artefact is caused by the temporal or spatial coherence of the X-ray beam, called 'phase contrast'. It can be explained as the refraction of the X-rays as they interact with the sample, causing edge enhancement effects. In some cases this effect is useful and can be used for phase contrast radiography⁸⁴. In many applications however, it makes phase segmentation challenging and reducing its effects is necessary. In laboratory μ CT, it mostly arises in cases of high resolution coupled with low attenuation. Phase contrast is strongly felt at synchrotron sources, due to the high coherence of synchrotron produced X-ray beams. Many processing and imaging methods exist that can benefit from this effect^{85,86}, or reduce it, depending on the desired application⁷⁴.

The above three artefacts are caused by either the imaging physics or by the mathematics of the reconstruction⁷⁴. Artefacts arising from faulty pixels, mechanical instability of the sample relative to the detector or high-density inclusions in the sample can also occur. Faulty pixels result in ring artefacts, where rings form as circles around the axis of rotation of the sample. Inclusions in the sample which have a high attenuation can result in streaks⁸⁷.

3.1.4. Data analysis and visualization

One of the main advantages of μ CT is its non-destructive, high-resolution 3D imaging ability. Its output is a 3D volume of the distribution of local linear attenuation coefficients. These are usually stored as a stack of 2D slices to ensure quick viewing is possible. The volume can then be visualized in terms of the linear attenuation coefficient, using specialised rendering software. Examples of such software are Fiji or Avizo. While this visual inspection is a useful tool for qualitative actions, dedicated software packages are needed to perform quantitative analyses on the 3D volume. The package most used during this dissertation was Avizo, but many other packages exist^{88–90}. Quantitative results produced from 3D analyses can include volume fractions of the present components, pore and grain sizes and other parameters such as shape factors, connectivity, etc. These parameters can then be used to conduct a statistical analysis on the entire 3D volume. 3D analyses are not straight forward, with imaging artefacts introducing systematic errors. Filtering of the images before conducting analyses is often required. User preference also introduces levels of uncertainty to these analyses, especially with operations such as thresholding of phases. This is the process whereby grey values within certain ranges are assigned as one phase in an attempt to segment the image into only the phases present, instead of a range of grey values. This step is necessary to conduct quantitative analyses. It is important that μ CT users take these uncertainties into account when conducting these analyses⁷⁴.

3.2. Experimental dataset

The dataset used in this dissertation was provided by Schlüter et al.⁸. The authors conducted unsteady state experiments on a cylindrical sample, made up of sintered soda lime beads of various diameters. 35% of the beads were 0.6 mm in diameter, 35% were 0.8 mm in diameter and the remaining 30% were 1.0 – 1.4 mm in diameter. The beads were contained within a quartz glass cylinder with an inner diameter of 5.8 mm. A porosity of 0.33 was achieved by packing the beads to a height of roughly 6 mm. The non-wetting fluid used was n-dodecane (referred to as oil in the results), while the wetting fluid used was brine. To ensure sufficient contrast when imaging the experiment, the brine was made up of a 1:6 mass ratio between caesium chloride (CsCl) and water. A hydrophilic nylon membrane was used at the bottom of the sample to act as a barrier, stopping the dodecane from entering the brine reservoir. A syringe pump filled with brine was connected to the bottom of the sample to control flow. Volumes measured with this pump were used to gather information on the wetting fluid saturation and converted to actual saturation values by determining the whole sample's reference volume. The dodecane reservoir was kept at atmospheric pressure, while the brine pressure was measured using an external pressure transducer. This ensured that any pressure transducer recordings represented the pressure difference between the fluids. This could then be equated to the capillary pressure at equilibrium conditions.

Very low flow rates were maintained for the duration of primary drainage and main imbibition cycles. The ratios between capillary forces and viscous forces (the capillary number), were 10^{-8} with the flow rates ranging from 20 – 50 μ l/h. This means that the flow was always near capillary equilibrium. These experiments were conducted at the Advanced Photon Source at the Argonne National Laboratory in the USA. The GSECARS beam line was used with a beam energy of 36.1keV to scan the sample during the experiment. Each scan took 113 seconds and was composed of 720 projections scanned over an angular range of 180°.

The acquired projections were reconstructed using a fast Fourier transform. A 3D image having a voxel size of 8.4 μm was produced. A volume of interest was selected for quantitative analysis, consisting of 84.7 mm^3 in 178 scans. Noise was removed by using a non-local means denoising filter⁹¹ in an attempt to remove noise while preserving true image features. A total variation denoising filter⁹² was then used to remove noise in the upper and lower regions of the image while not affecting the level of detail in the clearer centres of the images. Automatic image registration was then used to align all the images to a dry scan taken of the sample. A modified version of Markov random field segmentation was then used to segment the images into the three separate phases. Image artefacts arising from movement of the fluid interfaces during a scan (such as streakings seen in Figure 20) were eliminated. This was achieved by manually identifying such artefacts and replacing affected regions of the scan with scans from the previous or following timestep. The result was time-resolved μCT segmented images taken at discrete time intervals of primary drainage, main imbibition and main drainage showing the fluid distributions in the pore space at these times. For this dissertation, the 52 images of main imbibition were used for analysis as well as the 38 images of primary drainage used by Mascini et al.¹⁴. A summary of experimental parameters can be found in Table 1.



Figure 20: Streakings arising from fluid interfaces moving during a scan. The scale bar is 200 μm .

Table 1: Summary of the dataset used for image analysis of imbibition as well as for drainage.

	Imbibition	Drainage
Sample dimension	5.8 mm diameter x 7 mm long	5.8 mm diameter x 7 mm long
Boundary condition	Constant flow rate	Constant flow rate
Fluids	n-dodecane, CsCl-brine	n-dodecane, CsCl-brine
Interfacial tension	36 mN/m	36 mN/m
Flow rate	20 $\mu\text{l/h}$	50 $\mu\text{l/h}$
Capillary number	1×10^{-8}	4.2×10^{-8}
Number of timesteps	52	38
Time per time step	113 s	113 s
Time span (hr:min:sec)	2:37:16	1:13:44
Reconstructed voxel size	8.4 μm	8.4 μm
Pumped volume	54.1 μl	79.7 μl

3.3. Sensitivity analysis on image processing

In order to evaluate the impact of segmentation on geometric contact angle measurements, a sensitivity analysis using the method developed by Andrew et al.⁵⁸ was first performed. Since the dataset used for the main part of this dissertation consists of segmented images, a different dataset was used to investigate this: grey-scale μCT images with a voxel size of 2.5 μm of a Luxembourg Sandstone sample after drainage. Three different thresholding ranges were chosen for the dry image and the image after drainage respectively, resulting in nine different segmentations. A region of interest was chosen and a manual

geometric contact angle was measured at the same slice of all nine different segmentations. The resulting contact angle measurements exhibit a range of 28° (see Figure 21), showing that thresholding can introduce great uncertainty to the analysis. The Luxembourg Sandstone is a much more complex material than the glass beads, hence a smaller degree of uncertainty is expected in the latter.

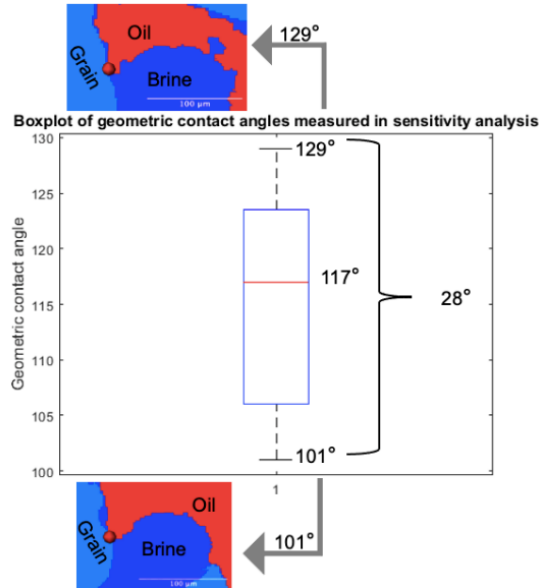


Figure 21: Boxplot showing the distribution of contact angle measurements due to differences in thresholding. The region examined showed oil-wet behaviour, despite the sample generally being water-wet.

3.4. Image analysis of imbibition

3.4.1. Identifying imbibition fluid displacement events

The first step in identifying displacement events is to divide the pore space into separate pores and throats, using a Pore Network Model (PNM). A PNM is a conceptual model which represents the pore space as a network of large voids, pores, which are connected by narrow passages, throats (see Figure 22), with idealized geometries. PNMs preserve the topology of the system. They indicate which pores (represented by nodes/balls) are connected to which other pores via throats (represented by links/cylinders). The balls and cylinders are only used for visual purposes. They can be assigned values for volume, inscribed radius, etc. depending on the underlying image¹⁹. They are also useful for modelling multiphase transport properties as they result in lower computational demands than simulating fluid distributions directly onto pore space images⁹³.

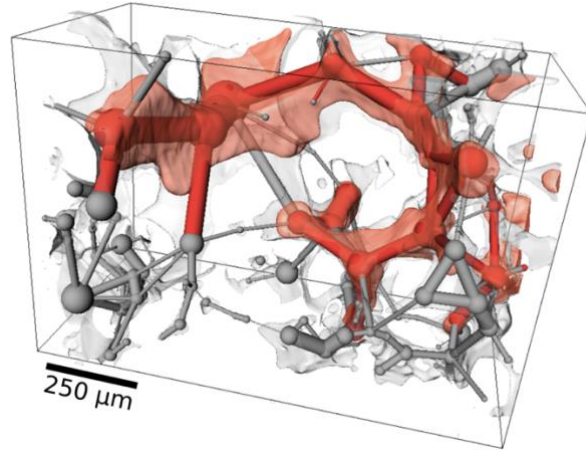


Figure 22: The transparent red phase is the non-wetting fluid. The PNM is shown by balls, representing pores and cylinders, representing throats. The balls and throats are colour coded to show which fluid is filling them. This is a snapshot of a subvolume imaged during an imbibition experiment⁹⁴.

The PNM used by Mascini et al.¹⁴ was used in this dissertation. “pnextract” (an open-source algorithm⁹⁵) was used to implement a watershed algorithm in order to find the maximum inscribed spheres in each pore and throat (Figure 23). The radius of the inscribed sphere is then assigned as the radius of that pore or throat. This PNM was used to conduct the upcoming analyses.

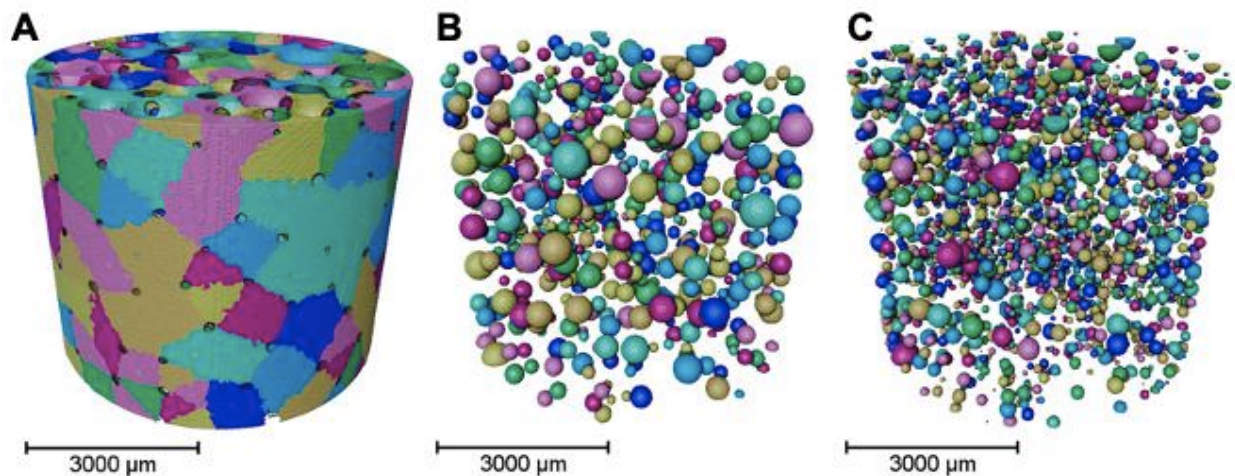


Figure 23: A) The PNM used during the analysis. B) The maximum inscribed spheres in the pores. C) The maximum inscribed spheres in the throats.

The method used for event identification is analogous to that used by Mascini et al.¹⁴. In order to assess the occupancy of each pore or throat, the maximum inscribed spheres of the PNM are overlain on the imbibition images, after they have been registered to the high-resolution dry scan of the sample. The occupancy of the pore or throat is then determined by whether the majority of voxels in the maximum inscribed sphere are brine or dodecane. This was done for every pore and throat in every timestep. This portion of the analysis was done in Avizo 2020.2 (Thermo-Fisher Scientific). Imbibition ‘fluid fillings’ were then identified when the occupancy of a pore changed from dodecane to brine in consecutive timesteps (i.e. in timestep ‘t-1’ the majority of voxels in the maximum inscribed sphere is dodecane, while in timestep ‘t’ the majority of voxels in the maximum inscribed sphere is brine). Fluid fillings that were connected and occurred in the same timestep were classified as part of the same event. In order to identify which pore fillings together constituted a single event, a connectivity clustering of the pores filled per timestep was

performed in MATLAB. The resulting adjacency matrix was used to identify pores which were filled in the same timestep and were connected and assign them to a single event. The pores and throats neighbouring those directly involved in the event were also recorded. The results of this analysis were a list of imbibition events, with various information (such as event times) recorded. The source pore for each event was determined by finding the pore neighbour with the largest radius. Analogous data was determined for drainage events by Mascini et al.¹⁴ using the above method.

During the course of this dissertation, a new algorithm to classify events into cooperative pore filling types and to identify snap-off was developed. To determine the co-operative pore filling type, the occupancy of the throats neighbouring the event was determined in the timestep prior to the event. If the event had one dodecane filled throat neighbour at timestep 't-1', it was classified as an I_1 event occurring in timestep 't'; if an event had two dodecane filled throat neighbours at timestep 't-1', it was classified as an I_2 event, and so on. Snap-offs were identified by locating throats that changed occupancy from dodecane filled to brine filled in consecutive timesteps, while the pores on either side of the throat in question remained dodecane filled. These analyses were conducted using MATLAB.

3.4.2. Geometric contact angles

The geometric contact angle was identified on every point on the three-phase-contact-line, using the fully automated method developed by AlRatrouf et al.¹³ with its default smoothing parameters. The algorithm generates a smooth 3D mesh and then identifies the three-phase-contact-line on this mesh. Geometric contact angles are calculated on every mesh point on the three-phase-contact-line by taking the dot product of the normal vectors to the solid surface and fluid/fluid interface at this point (see Figure 24). Using this data and the PNM, the geometric contact angle was found for every pore at every timestep. The geometric event-based contact angles were determined by taking the geometric contact angles in the event pores as well as in the neighbouring pores in the timestep prior to the displacement event and calculating a weighted average. The global geometric contact angle was also determined using all the geometric contact angles in the entire image of the final timestep, in order to make comparisons. Geometric event-based as well as global geometric contact angles for drainage were determined by Mascini et al.¹⁴ using the same method.

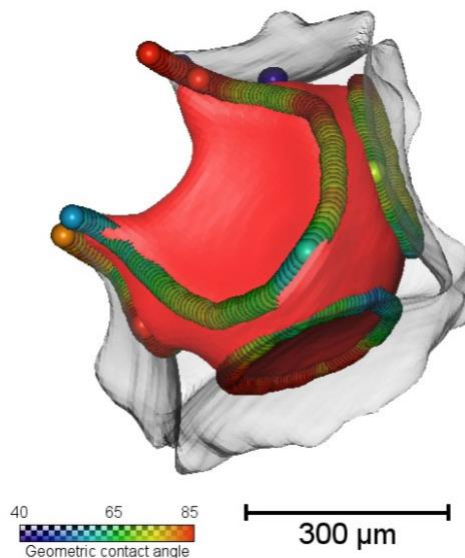


Figure 24: Visualization of a pore, showing the geometric contact angles calculated by automated methods as a point cloud. The red volume is dodecane, the transparent grey structure is the pore and the brine is not visualized.

3.4.3. Capillary pressures and force-based contact angles

The force-based contact angles for each event were calculated by determining the mean curvature for the event one timestep prior to the event occurring. This curvature was then used to calculate the capillary pressure which triggered the event. Coupling this with the radius of the source pore yields an estimate of the force-based contact angle of the imbibition event.

In order to determine curvatures, the fluid/fluid interface was extracted from the three-phase segmented image as a triangulated surface, by making use of the marching cubes algorithm⁹⁶ in Avizo 2020.2. This algorithm uses millions of triangles to approximate a smooth surface between the two fluids. The resolution of the image determines the number of triangles generated, with higher resolutions corresponding to more triangles. After the image was labelled, the surface generation module in Avizo was used to generate the surface and perform constrained smoothing, which means that voxel labels stayed the same, i.e. any two voxels that were labelled differently prior to smoothing now had a surface between them after the surface generation. A smoothing extent of three voxels was used in combination with a Gaussian filter. This method is analogous to that used by Mascini et al.¹⁴ as well as Li et al.²³.

A quadratic form was then fitted to the surface locally, the eigen vectors and eigenvalues of which were used to calculate the mean surface curvature. This computation is limited in accuracy due to image resolution⁵⁷, especially in regions where the partial volume effect is particularly pronounced, such as near the three-phase-contact-line^{14,23}. In order to account for this limitation on accuracy, the data points of curvature were filtered based on two criteria. All curvature data points with a radius of curvature less than two times the reconstructed voxel size were omitted. This was done because these curvatures were deemed more likely to be strongly impacted by noise. Another filtering method was then employed to lessen the effects of image quality near the three-phase-contact-line specifically: this involved setting a threshold geodesic distance from the grain surface. Any curvature data points too close to the surface edge (< 20% of the maximum geodesic distance of the interface on which they are found), were omitted from the calculation (see Figure 25). These geodesic distances were determined using the shortest edge distance algorithm developed by Dijkstra⁹⁷. The remaining data points were weighed based on their geodesic distance from the edge of the surface. The mean surface curvature was then used to calculate the mean threshold capillary pressure. This in turn was used along with the pore radius of the source pore to calculate the force-based contact angle. This method can only be used to determine the force-based contact angles of I_1 events. Force-based contact angles for drainage were determined by Mascini et al.¹⁴ using this same method.

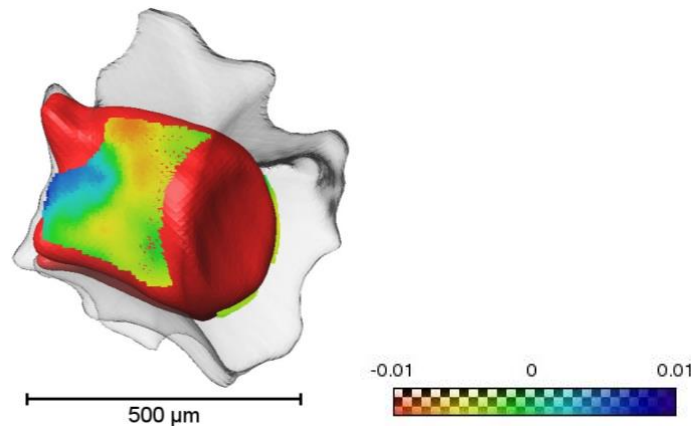


Figure 25: Visualization of filtered curvature values used to calculate mean surface curvatures. The red volume is dodecane, the transparent grey structure is the pore and the brine is not visualized.

In order to calculate the force-based contact angles of I_n type events where $n \geq 2$, the cooperative pore body filling model developed by Ruspini et al.⁹⁸ was implemented. This model is only valid for events which are one pore in size, hence it was only used for events matching this characteristic. This model accounts for the geometrical characteristics of the pore, the spatial distribution of neighbouring pore throats as well as the local fluid topology at the moment of the displacement. The inputs to the model for each event are the radii and locations of the centres of the event pore and neighbouring dodecane-filled throats, as well as the event-based geometric contact angle. The model returns the equivalent threshold capillary pressure which can be used to calculate the force-based contact angle.

3.4.4. Thermodynamic contact angles

In order to calculate the thermodynamic contact angles for each imbibition event, the work done by Mascini et al.¹⁴ and by Blunt et al.¹⁵ was extended by using Eq. 6, where DV_1 is the change in brine volume during the event and $DA_{1,s}$ is the change in brine/solid surface area. The extracted triangulated surfaces described in section 3.4.3 were used to calculate the change in surface areas of the brine/solid surface interface for each event. The curvatures, saturations and surface and volume changes per event were used to reach an event-based thermodynamic contact angle, which could then be compared to the geometric event-based contact angles and force-based contact angles. The thermodynamic contact angle for the entire experiment using the first and last timesteps was also determined in order to make comparisons. Event-based thermodynamic contact angles as well as the thermodynamic contact angle for the entire drainage experiment were determined by Mascini et al.¹⁴ using the same methods.

3.4.5. Validation and verification

In order to verify and validate the methodology used, a number of events were visualised in Avizo. The event times and I_n types were evaluated to determine whether the computed filling times and dodecane filled neighbouring pores were correctly predicted. Manual geometric contact angle measurements were made to assess their agreement to the automated geometric contact angles calculated. Curvatures were visualized to determine whether the fluid/fluid interface curvatures were physically feasible and to ensure no errors or artefacts were corrupting the data. Curvature-based capillary pressures were compared with experimental capillary pressures as a further form of validation.

4. Results

In the following section, the results of this dissertation will be put forward. First, case studies of specific fluid displacement events will be examined to obtain an intuitive understanding of how geometric contact angles, curvatures and surface areas of interfaces changed with time. Then, statistics on all fluid displacement events in the experiment will be examined, including the global curvatures, capillary pressures, global volumes and surface areas and the different types of contact angles. Finally, imbibition will be compared to drainage so as to later quantify hysteresis.

4.1. Case studies of single event results

4.1.1. Piston-like filling

In describing the results, we refer to I_1 events as piston-like fillings as the terminal meniscus moves through the centre of the pore in a manner analogous to a Haines jump moving through a throat during drainage³⁰. A rendering of such an event in the experimental dataset, which is referred to as Event 1, can be seen in Figure 26. Two snap-offs have occurred at earlier times, disconnecting the oil in the pore which would later be filled from the oil in two of the neighbouring pores. The oil was then displaced by the advancing brine through the last oil-connected throat. "Event neighbourhood" refers to the pore(s) filled during the event as

well as the pores directly surrounding those which were filled during the event. The mean of the geometric contact angles in the event neighbourhood was found for each timestep in which there were contact lines present (47 timesteps out of 52) and plotted as a function of time (Figure 27). The surrounding pores were included since these were also used to determine the event-based contact angles, and because increasing the volume in which measurements are averaged counteracts the uncertainties on the PNM extraction that was used to identify individual pores. The mean curvatures of the event neighbourhood were also calculated (Figure 27) as well as the sum of the surface areas of the rock/brine, rock/oil and oil/brine interfaces in the event neighbourhood (Figure 28).

Event 1

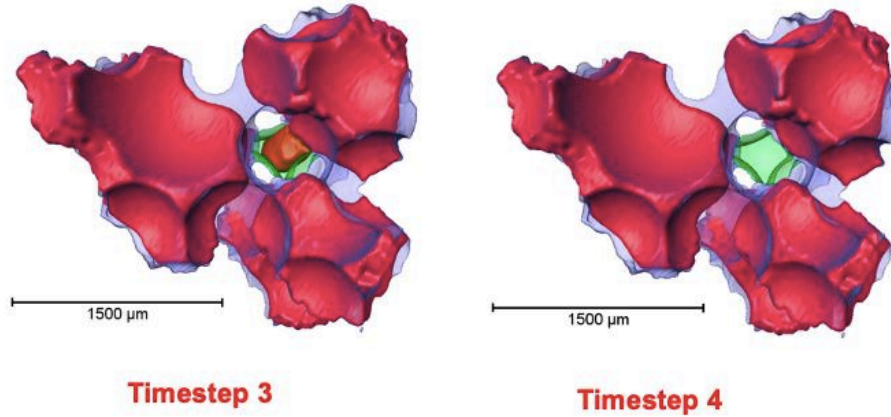


Figure 26: A rendering of event 1. The pore filled during the event is green, while the pores neighbouring the event are purple. The oil is red and the brine has not been visualized.

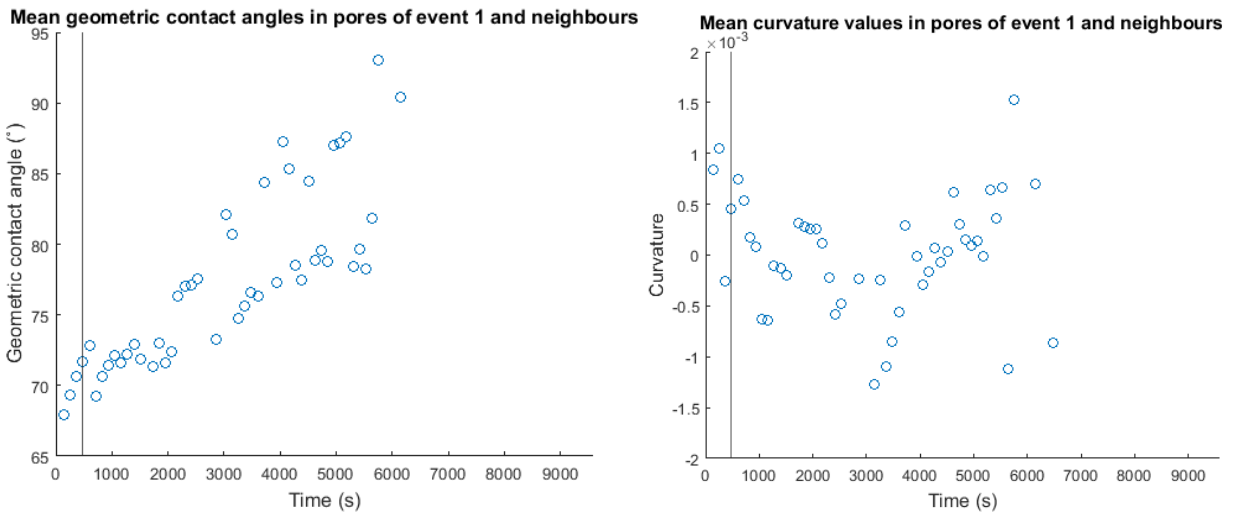


Figure 27: Left: Mean geometric contact angles in the event 1 neighbourhood. Right: Mean curvatures in the event 1 neighbourhood. The vertical line demarcates the time at which the event occurred, which corresponds to timestep 4.

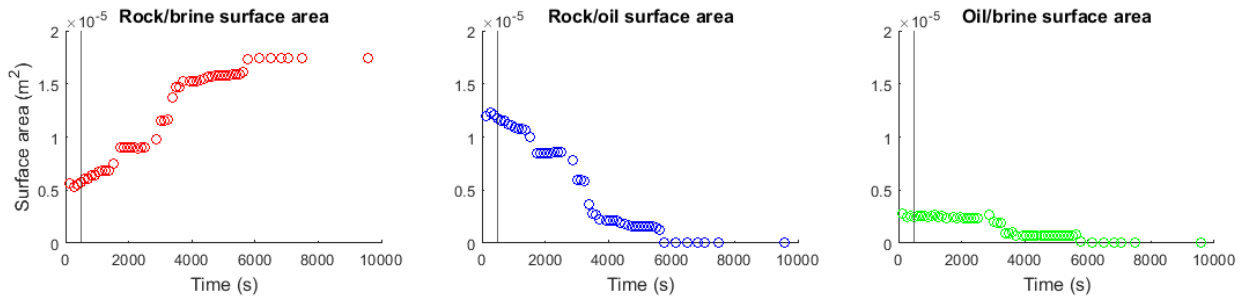


Figure 28: Sum of the surface areas in the event 1 neighbourhood. The vertical line demarcates the time at which the event occurred, which corresponds to timestep 4 in the μ CT series.

Event 2

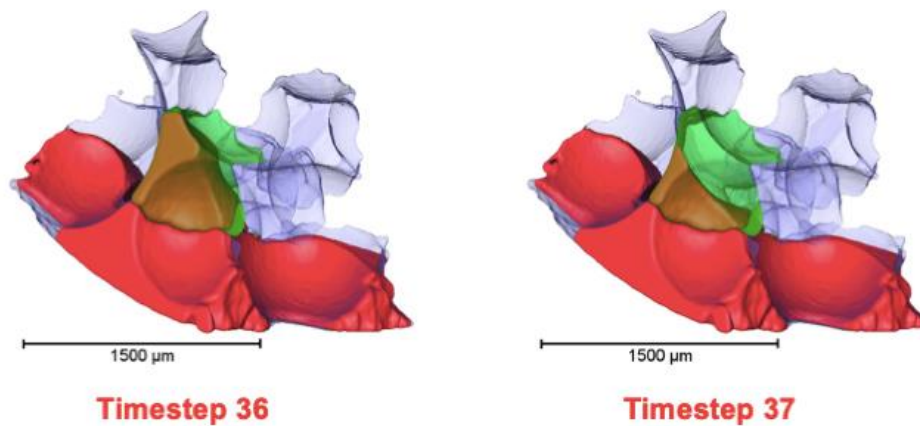


Figure 29: A rendering of event 2. The event pore is green, while the pores neighbouring the event are purple. The oil is red and the brine has not been visualized.

A second piston-like filling event, referred to as Event 2 can be seen in Figure 29. In this example, the pore filled during the event did not become completely filled with brine, but was still classified as an event as more than half of the pore became brine-filled. The mean geometric contact angles for the event neighbourhood increase with time, while the mean curvatures decrease (Figure 30). The summed surface areas for the different interfaces can be seen in Figure 31. For this event, averages could be calculated for all 52 timesteps.

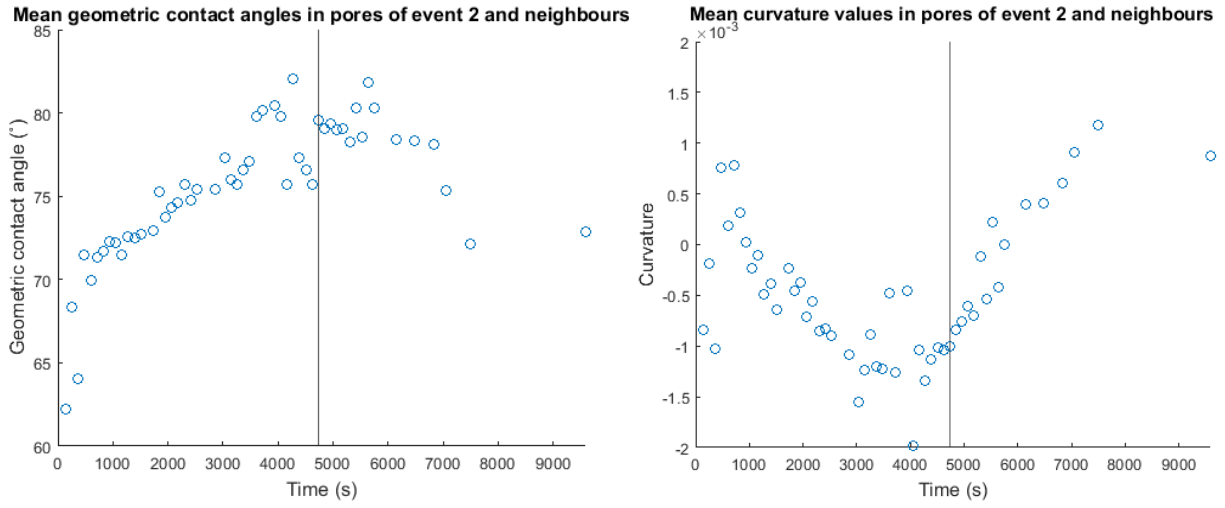


Figure 30: Left: Mean geometric contact angles in the event 2 neighbourhood. Right: Mean curvatures in the event 2 neighbourhood. The vertical line demarcates the time at which the event occurred, which corresponds to timestep 37.

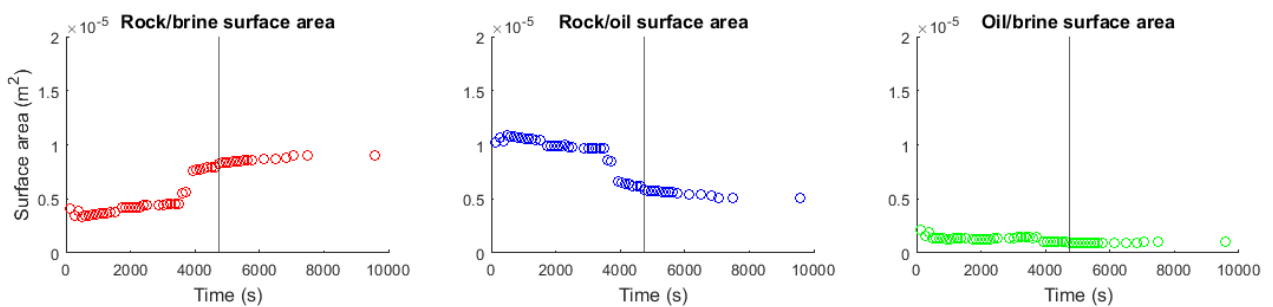


Figure 31: Sum of the surface areas in the event 2 neighbourhood. The vertical lines demarcate the time at which the event occurred, which corresponds to timestep 37.

4.1.2. Cooperative pore filling

Event 3

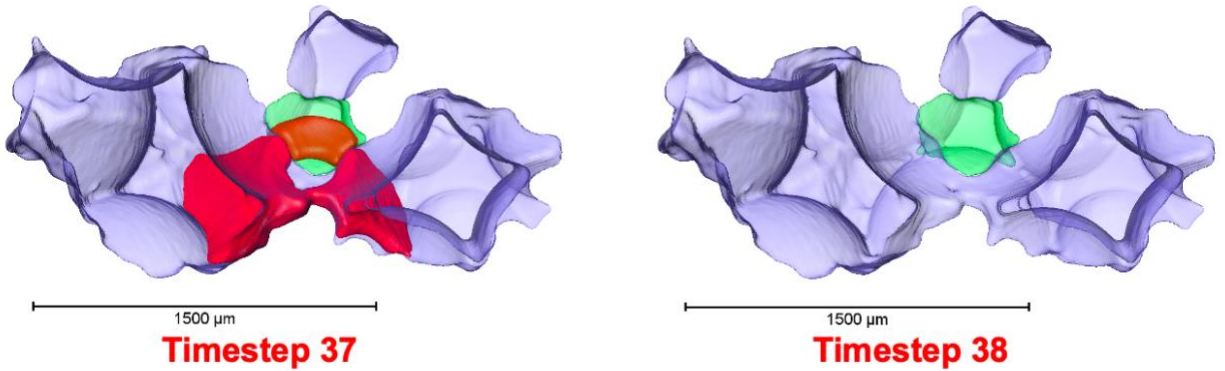


Figure 32: A rendering of event 3. The event pore is green, while the pores neighbouring the event are purple. The oil is red and the brine has not been visualized.

The third event we consider is a cooperative pore filling of a pore that was connected to three throats, of which two were filled with oil in the timestep preceding the event (Figure 32). The oil was displaced out of the event pore by the advancing brine, through the two remaining oil-filled throats. The mean geometric contact angles for the event neighbourhood increase with time, while the mean curvatures decrease (Figure 33). The summed surface areas for the different interfaces can be seen in Figure 34. For this event, averages could be calculated for 37 timesteps.

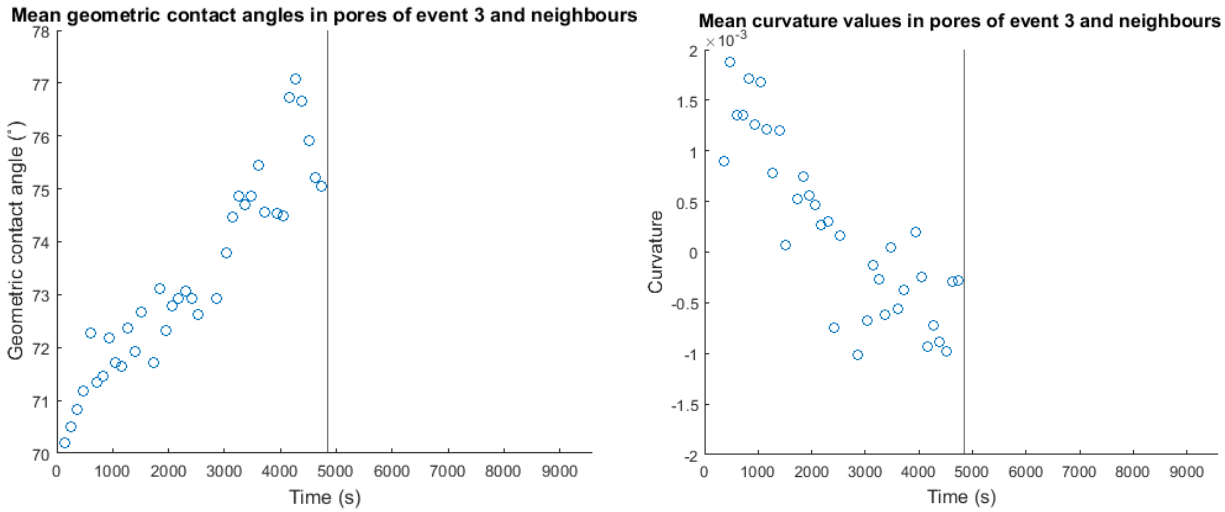


Figure 33: Left: Mean geometric contact angles in the event 3 neighbourhood. Right: Mean curvatures in the event 3 neighbourhood. The vertical line demarcates the time at which the event occurred, which corresponds to timestep 38.

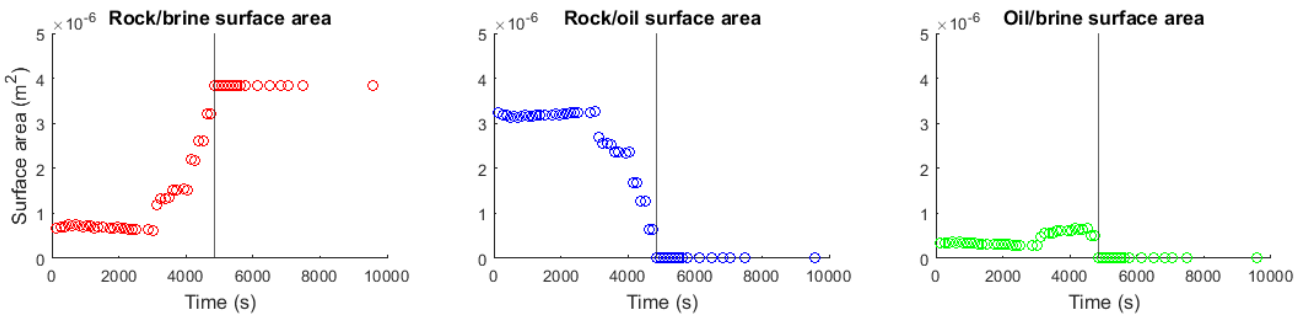


Figure 34: Sum of the surface areas in the event 3 neighbourhood. The vertical lines demarcate the time at which the event occurred, which corresponds to timestep 38.

4.1.3. Snap-off

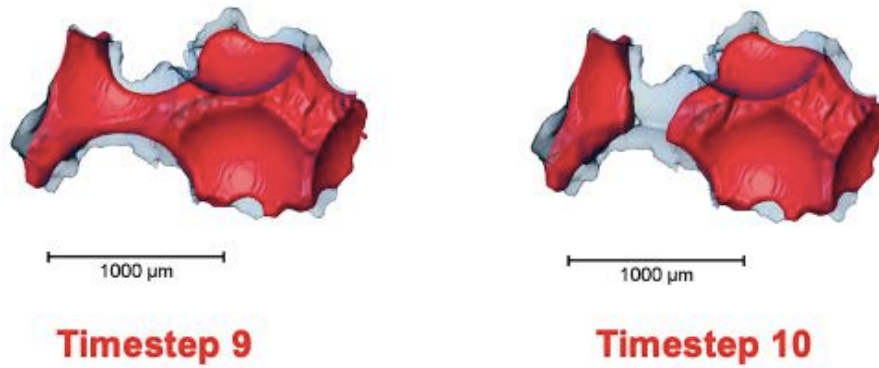


Figure 35: A rendering of a snap-off. The pores are blue, while the oil is red and the brine has not been visualized.

A rendering of a snap-off event can be seen in Figure 35. The mean geometric contact angles and the mean curvatures in the pores neighbouring the throat in which the snap-off occurred both increase with time (Figure 36). The summed surface areas for the different interfaces can be seen in Figure 37. For this event, averages could be calculated for 25 timesteps.

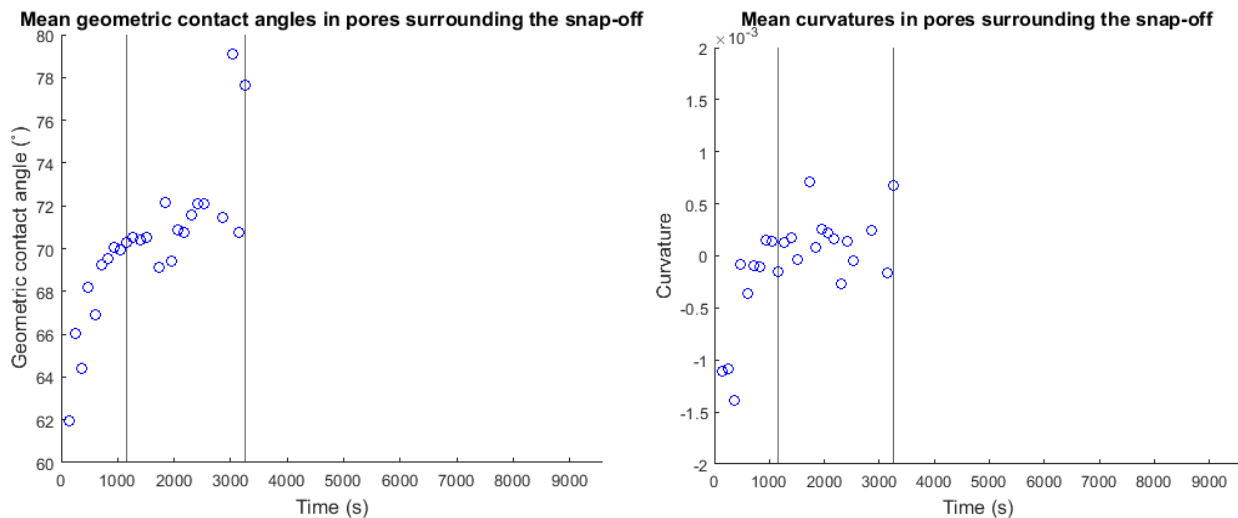


Figure 36: Left: Mean geometric contact angles in the pores adjacent to the snap-off. Right: Mean curvatures in the pores adjacent to the snap-off. The first vertical line shows the time of snap-off (timestep 10), while the second vertical line shows the time at which both adjacent pores became brine-filled (timestep 25).

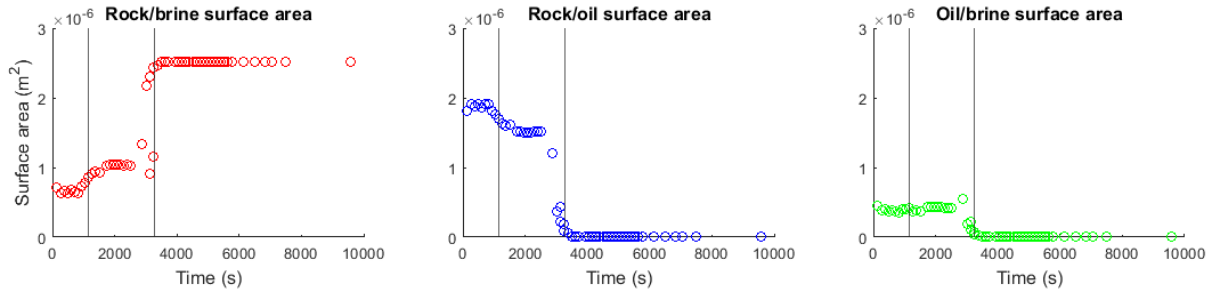


Figure 37: Sum of the surface areas in the pores adjacent to the snap-off. The first vertical line shows the time of snap-off (timestep 10), while the second vertical line shows the time at which both adjacent pores became brine-filled (timestep 25).

4.2. Pore filling statistics

After analysing how the properties of the selected fluid displacement events in Section 4.1 evolved over time, the following section will investigate the statistics of the displacement events in the entirety of the experiment.

4.2.1. Event overview

By detecting changes in pore occupancy during the experiments and then clustering these changes into specific events, 133 events were detected during the imbibition experiment (Table 2). Up to 11 events and 3 multi-pore events were detected in a single timestep (Figure 38). A vast majority of events consisted of a single pore being filled, with the frequency of occurrence generally decreasing as the number of pores invaded per event increase (Figure 38).

Table 2: Overview of detected events.

Number of identified events	133
Number of multi-pore events	52
Number of pores in largest event	16
Number of snap-offs identified	45

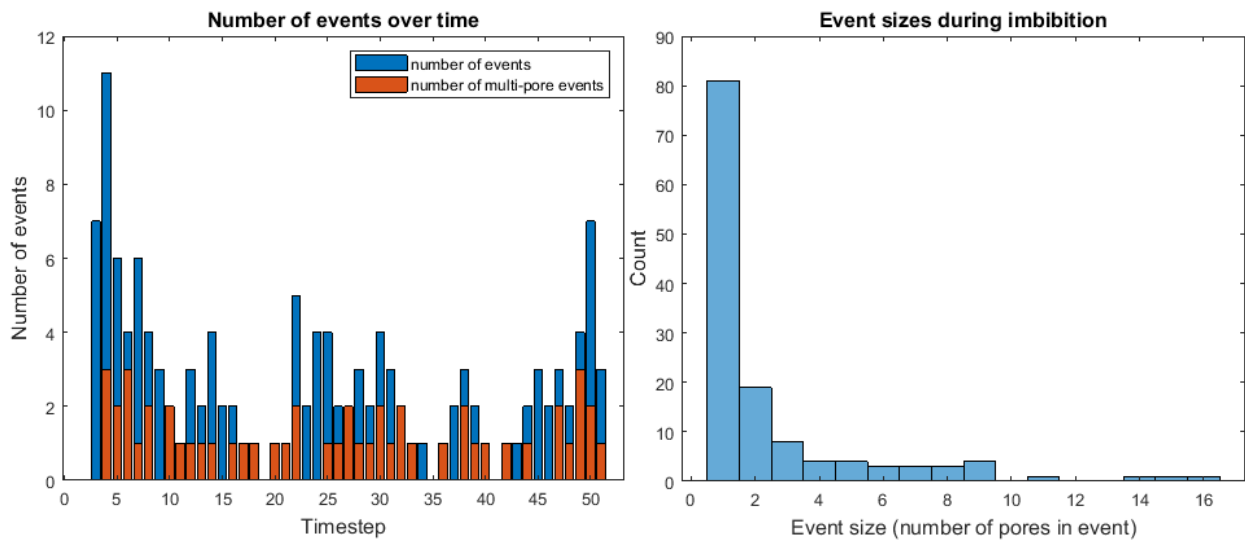


Figure 38: Left: The number of events detected is plotted per timestep. Multi-pore events are shown in red. Right: A histogram of event sizes.

Traditionally, I_n event classification is based on the filling of a single pore, with n oil-filled neighbouring throats³⁰. Due to limited time resolution, I_n classification here is based on counting the number of neighbouring oil-filled throats to every pore invaded during the event, which, as shown in Figure 38, can consist of a multitude of pores. This likely results in an overestimation of the n in the classification of multi-pore filling events. For this reason, the distribution of the I_n types of single-pore events was considered separately from all events, both of which can be seen in Figure 39. The majority of all events were either piston-like fillings or I_2 , I_3 or I_4 events. The event type of the highest prevalence was I_2 . Events of type I_8 and higher were grouped together and made up 19% of events overall. A total of 81 events were only one pore in size. There were 12 piston-like events, all of which were one pore in size. Up to 4 snap-offs were detected in a single timestep (Figure 40).

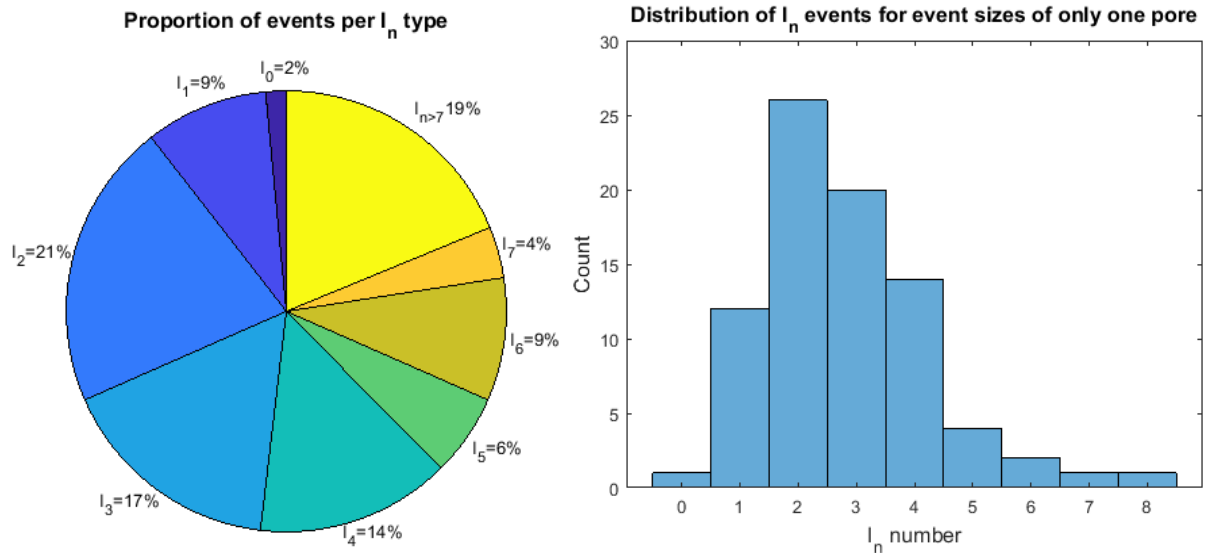


Figure 39: Left: A pie chart of the percentage of events of each I_n type. 'n' refers to the number of throat neighbours that were oil-filled in the timestep preceding the event. Right: Proportion of event I_n types for events which are only one pore in size.

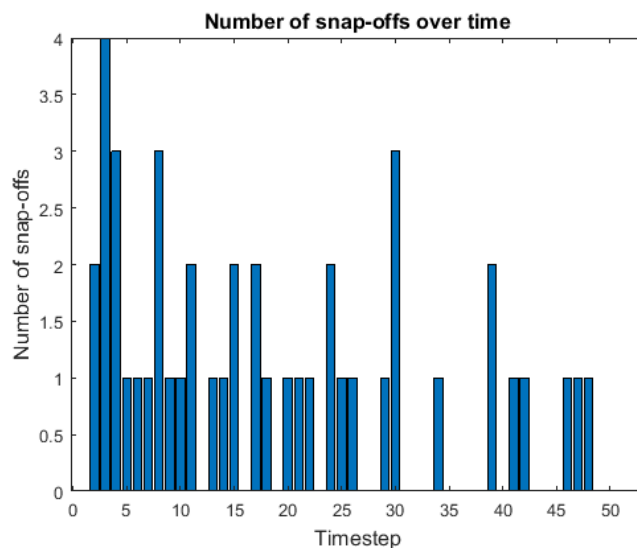


Figure 40: A bar chart of snap-offs per timestep.

4.2.2. Global curvatures

Using the method described in the Section 3.4.3, the average curvatures were found for each timestep (Figure 41). The reported curvatures were clipped and weighted based on their geodesic distance from the grain surface. These measurements were indicative of the entry capillary pressures and were used to calculate force-based contact angles.

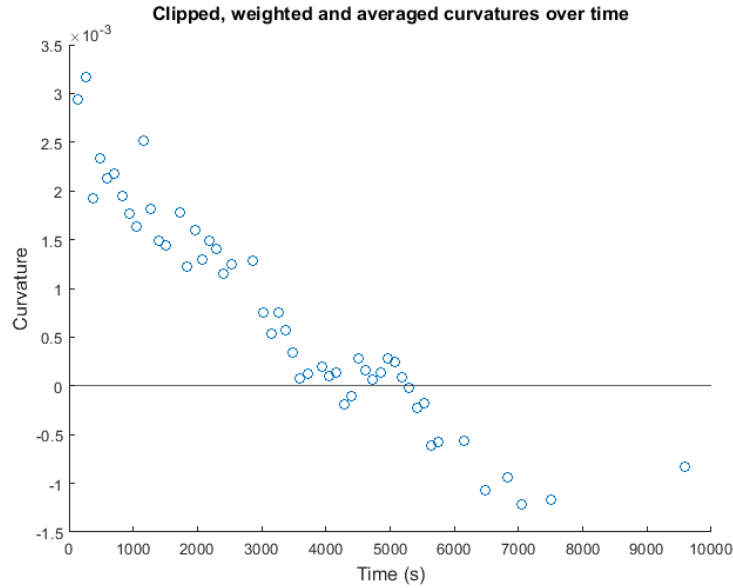


Figure 41: Plot of mean geodesic curvatures. These values have been clipped and weighted. A horizontal line at zero has been plotted to highlight when the values become negative.

4.2.3. Capillary pressures

The entry capillary pressures of piston-like fillings (Figure 42) were used to calculate force-based contact angles. These events were also more directly comparable to drainage events and have hence been considered separately from the other events. The entry capillary pressures for all events can also be seen in Figure 42. Capillary pressures determined from curvatures were compared to external pressure transducer measurements and to a cooperative pore filling entry pressure model based on the local pore geometry by Ruspini et al.⁹⁸. The curvature based capillary pressures were further grouped based on I_n event type and were also plotted for events only one pore in size (Figure 43). Only four events out of 81 single-pore filling events were larger than I_5 . This was done to better understand single pore events of I_2 type or higher, since the model put forward by Ruspini et al.⁹⁸ is only suitable for single-pore filling events.

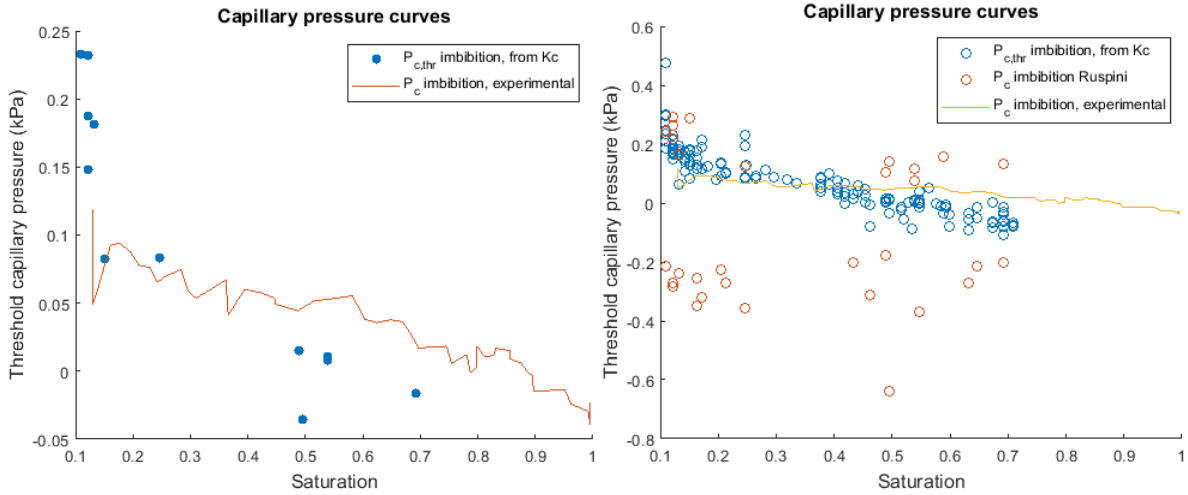


Figure 42: Left: Capillary pressure curve for piston-like fillings, based on curvatures (K_c) along with experimentally determined pressures. Right: Capillary pressure curves for all events, based on curvatures (K_c), the model developed by Ruspini, et al.⁹⁸ and experimental values.

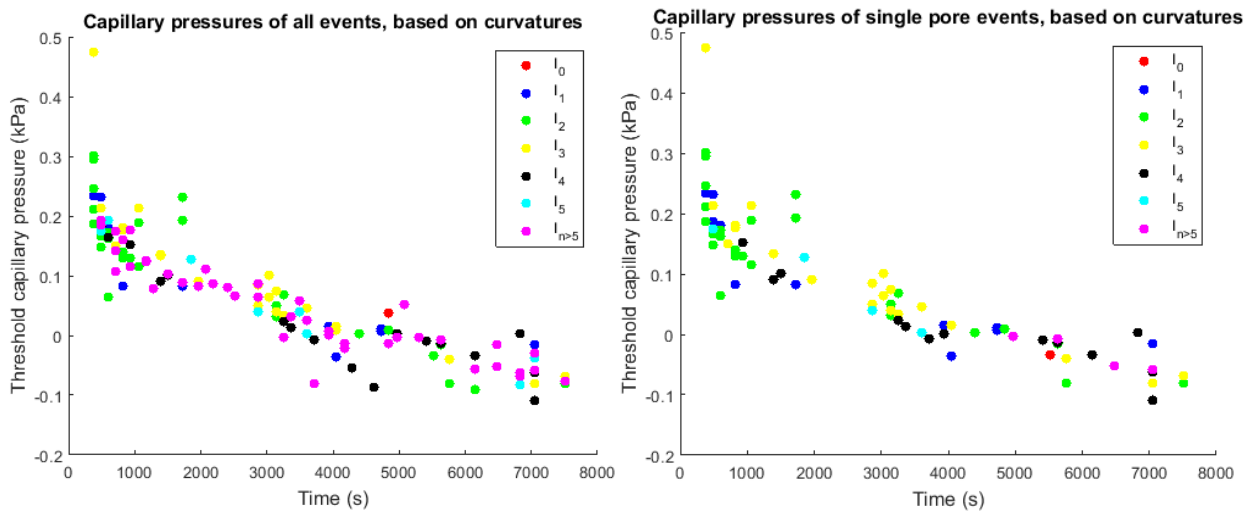


Figure 43: Left: Capillary pressures based on curvatures, grouped by I_n event type. Right: capillary pressures for events only one pore in size, based on curvatures and grouped by I_n event type.

4.2.4. Volumes and surface areas

The volume of brine which displaced oil in each event was determined and standardised to the total brine volume change in the entire experiment (Figure 44). This was plotted as a function of time, and colour coded based on event size. The total surface areas of the rock/brine, rock/oil and oil/brine interfaces were

also determined (Figure 45). These parameters were determined for each individual event in order to compute the associated thermodynamic contact angles.

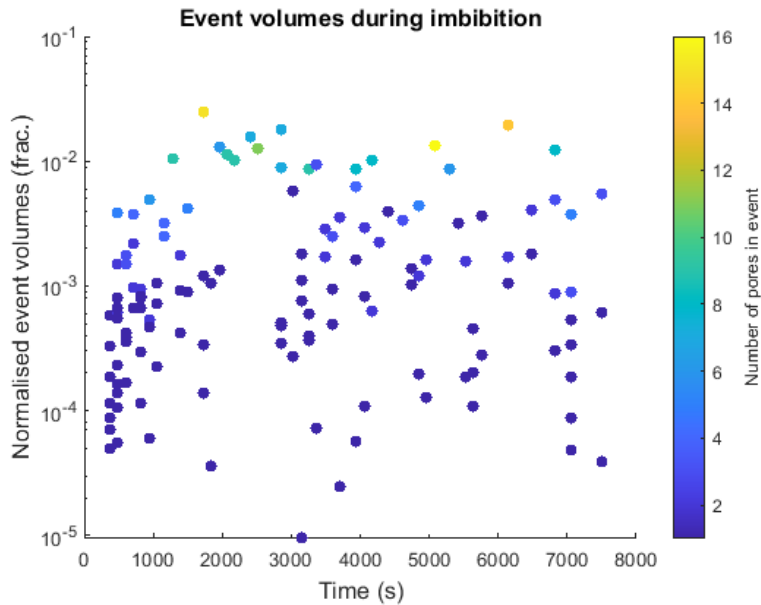


Figure 44: A plot showing the normalised volume of each event, with the number of pores filled in the event as colours.

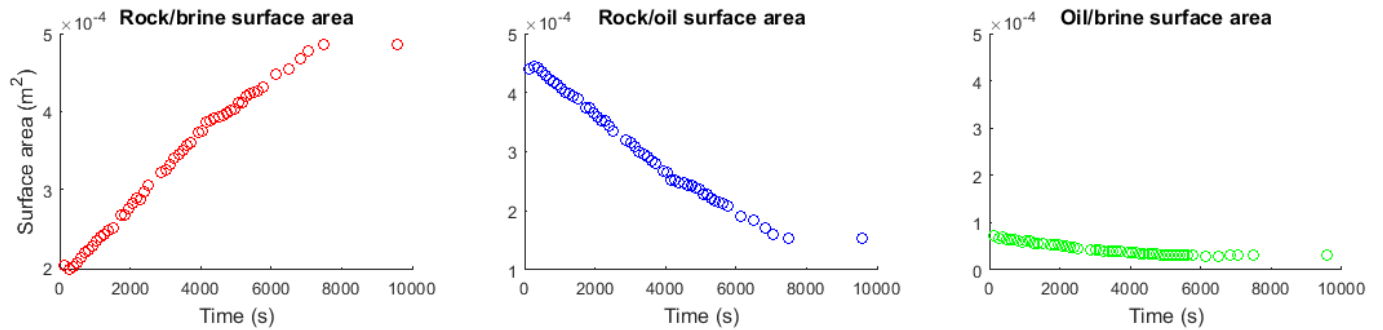


Figure 45: Total surface areas of the rock/brine, rock/oil and oil/brine interfaces.

4.2.5. Geometric, event-based, force-based and thermodynamic contact angles

The distribution of geometric event-based contact angles can be seen in Figure 46 in red. Values span 15° , ranging from approximately 66° to 81° . The mean geometric event-based contact angle for the whole experiment is 72° . The values have also been grouped according to event type (Figure 47).

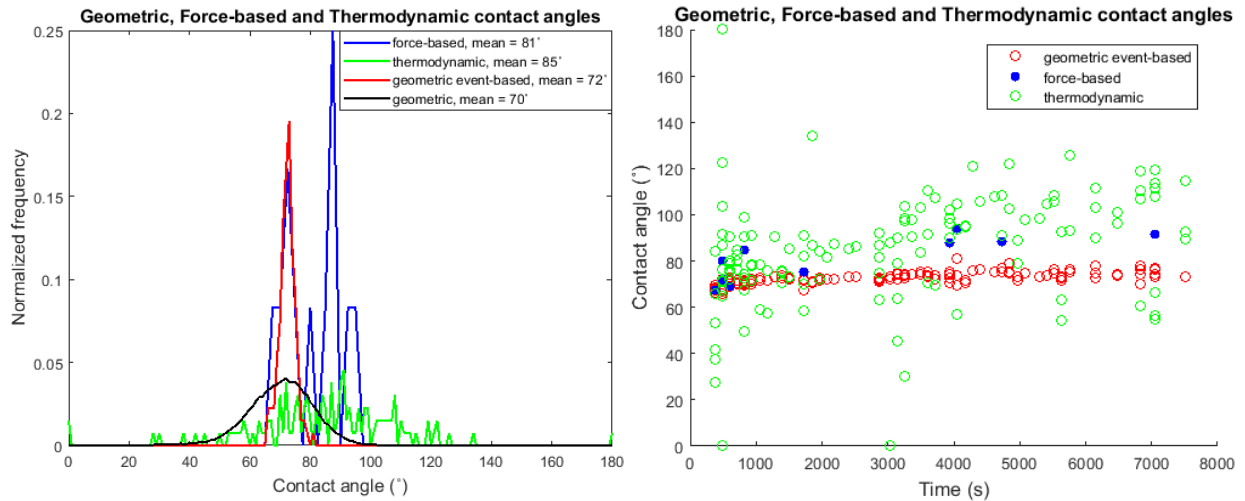


Figure 46: Left: Frequency distributions of different types of contact angles. Right: Contact angles plotted against time. Force-based contact angles are only calculated for piston-like events.

The distribution of the global geometric contact angles can be seen in Figure 46 in black. These are the ‘static’ counterpart of the geometric event-based contact angles and are made up of the contact angle measurements in the entire sample in the final timestep of the experiment. The range of these values is roughly 159°, with the minimum being 3° and the maximum being 162°. The mean is 70°.

The distribution of force-based contact angles can be seen in Figure 46 in blue. Values span 27°, ranging from approximately 67° to 94°. The mean force-based contact angle for the whole experiment is 81°. The Young-Laplace method of calculating contact angles by using the curvature to estimate capillary pressure is only valid for piston-like events, hence the force-based contact angles were only determined for these 12 events, resulting in a rather noisy distribution.

The distribution of thermodynamic contact angles can be seen in Figure 46 in green. Values range all the way from 0° to 180°. The mean thermodynamic contact angle for the whole experiment is 85°. The method used by Blunt et al.¹⁵ to calculate a single “average” thermodynamic contact angle for the entire experiment was also used and a value of 87° was obtained. This uses the difference in volumes and surface areas between the first and last images of the experiment.

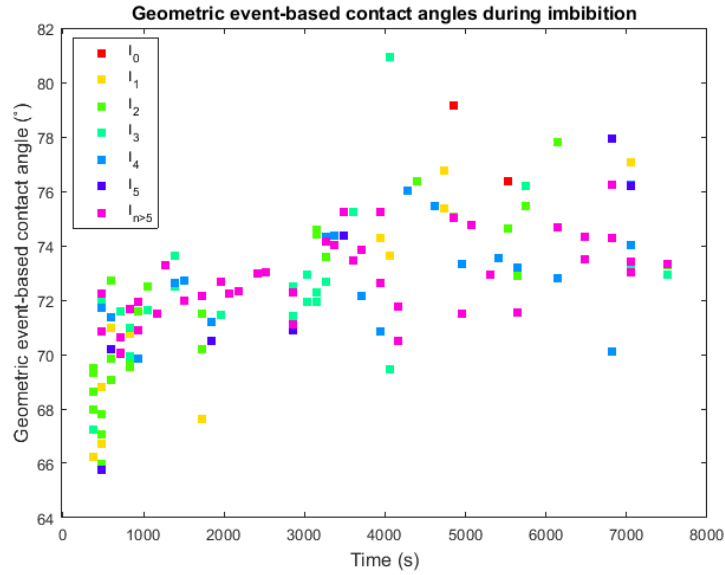


Figure 47: Geometric event-based contact angles grouped by I_n event type.

4.3. Comparison between imbibition and drainage

Capillary pressure curves for imbibition and drainage based on curvatures as well as experimental data were plotted (Figure 48).

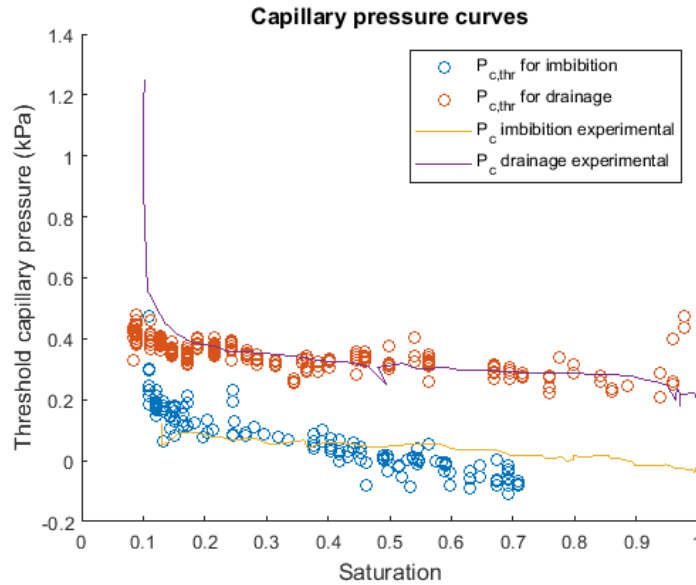


Figure 48: Each $P_{c,thr}$ is calculated from the curvature measurements during imbibition and drainage respectively. The experimental measurements were made with an external pressure transducer.

Each pore was assigned the geometric event-based contact angle of the event it was filled in. This was done for imbibition and drainage so that these values could be compared to assess contact angle hysteresis (Figure 49). The data was grouped in terms of the event type. The mechanism of piston-like events is

directly comparable to the Haines jumps of drainage, hence pores that were filled by these events are of special interest (Figure 49).

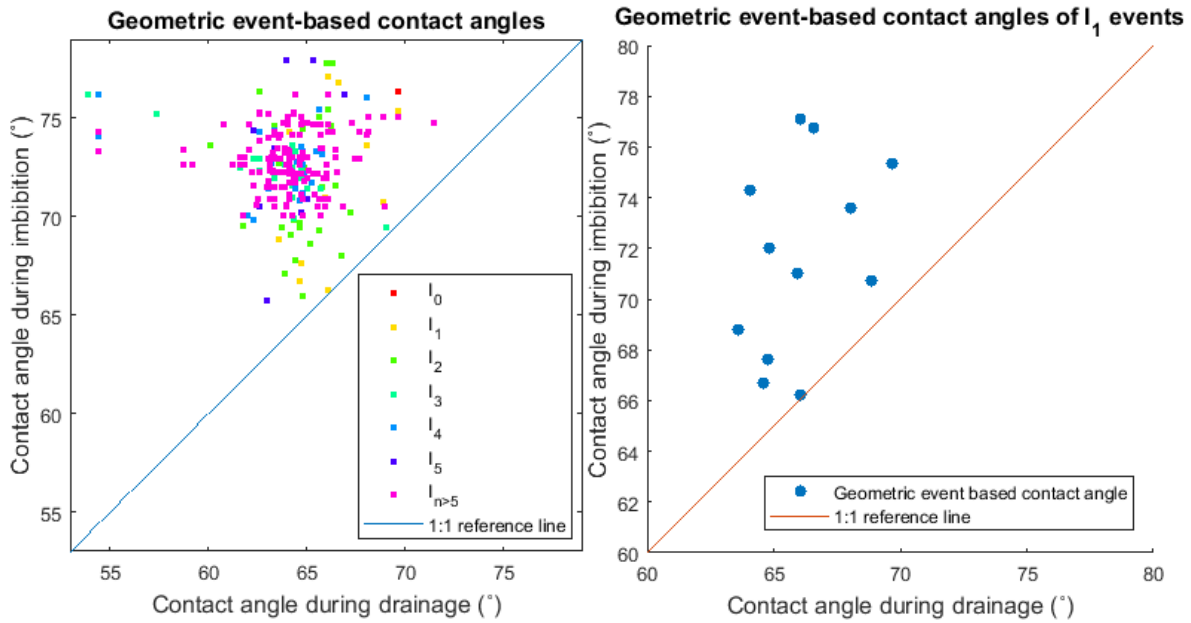


Figure 49: Left: Geometric event-based contact angles during imbibition plotted against the values seen during drainage. This is done on a pore-by-pore basis. Right: Geometric event-based contact angles of I_1 events during imbibition plotted against the corresponding pores during drainage.

There is a negative trend between the pore filling order of piston-like events during imbibition and the filling order of the corresponding pores during drainage (Figure 50). This is expected since pores that filled last during drainage are expected to fill first during imbibition.

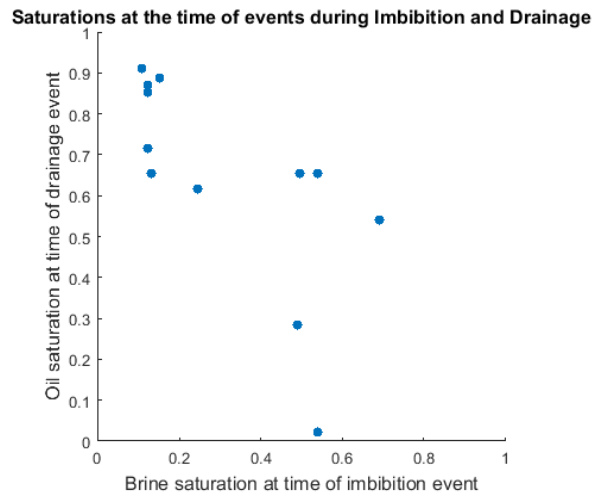


Figure 50: A plot of the saturations when piston-like events occurred during imbibition and saturations when the same pores were filled during drainage.

5. Discussion

In the following section, the Results will be analysed and interpreted. First, the validation and verification of event detection and classification, contact angle measurements and curvature measurements will be addressed. Then, the Case studies of single event results will be discussed followed by the Pore filling statistics for the entire experiment.

5.1. Validation and verification

5.1.1. Manual geometric contact angle measurements

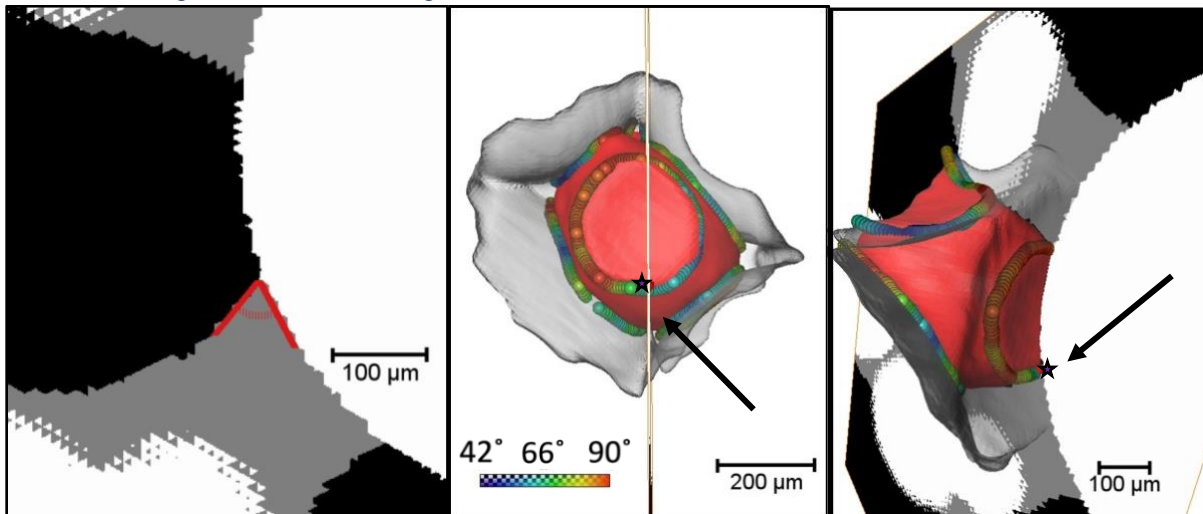


Figure 51: Left: a manual geometric contact angle measurement of 67° taken in the pore of event 1 at 372 seconds. Centre: the line is the plane on which the contact angle was measured. The coloured circles show the geometric contact angles calculated by the automated algorithm. Right: a different point of view of the plane of measurement. The purple star shows the point that the manual angle was measured at. The plane was selected to be perpendicular to the three-phase-contact-line at the point of measurement. The manual contact angle measurement is in good agreement with the automated contact angles.

In total, six manual geometric contact angles were measured, three for event 1 and three for event 3 (one of these can be seen in Figure 51). Most were in good agreement with the automated geometric contact angles, validating the algorithm used. Five of the measurements varied from the calculated contact angle by 3° or less, with only one varying by 15° . The segmented images were used for these manual measurements. In the ideal situation, the grey-scale images would have been used to measure the geometric contact angles manually, but these were not available, hence the less ideal segmented images were used.

5.1.2. Event visualization

The renderings of the events were used to verify that the event times and I_n type of events that were automatically determined were correct. These can be seen in Figure 26, Figure 29 and Figure 32. Two I_0 events were detected. This suggests that the oil in the involved pores was already disconnected from the oil in the rest of the pore space before the event occurred, yet still managed to be displaced out of those pores. These events were visualised to assess what was actually happening (Figure 52). It was determined that the pores were at the edge of the field of view, and the oil was escaping to outside the field of view,

meaning the algorithm worked as expected. Further inspection renderings were made, but were not included here for brevity.

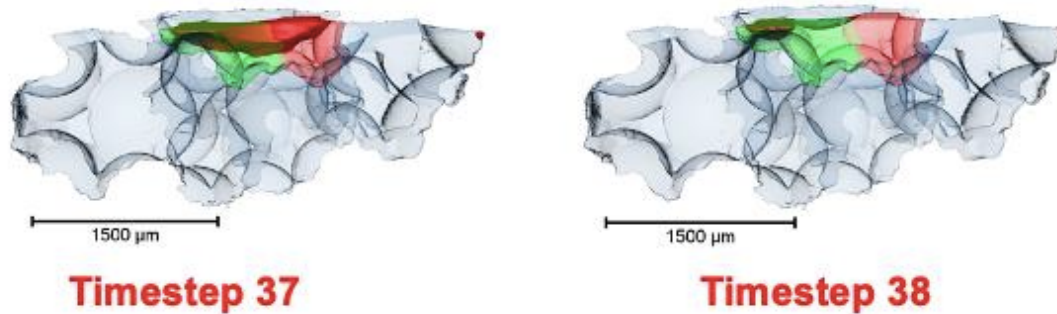


Figure 52: Rendering of an I_0 event, showing the involved pores are at the edge of the image and the oil is being displaced to outside the field of view. The pores of the event are green and red. The neighbouring pores are blue. The oil is red and the brine is not visualized.

5.1.3. Capillary pressures

The interfacial curvature measurements are integral to the calculation of the force-based contact angles as well as the calculation of the curvature-based capillary pressures. To validate the curvatures, the calculated capillary pressures were compared with the pressures determined by the external pressure transducers during the experiment. The experimentally determined capillary pressures and saturations were plotted alongside the capillary pressures and saturations determined from the images as capillary pressure curves (Figure 42 and Figure 48). As seen in these figures, the calculated pressures align fairly well with the experimental pressures, with some scatter. This is expected, due in part to limited spatial and temporal resolution. Since the experiment was of unsteady-state flow, scatter could be further caused by local variations in capillary pressure, since equilibrium was not reached. Considering all of this, the measured pressures and calculated pressures are in good agreement.

5.2. Case studies of single events

5.2.1. Geometric contact angles and curvatures

The geometric contact angles of all the case study events increase until the event occurs, after which they either continue to increase (as in Event 1), decrease (as in Event 2), have no further values (as in Event 3) or plateau (as in the example Snap-off). The interfacial curvatures of events 1, 2 and 3 decrease until the event occurs, whereas the interfacial curvatures surrounding the snap-off increase until the snap-off event occurs. They then either continue decreasing (as in Event 1), increase (as in Event 2), have no further values (as in Event 3) or plateau (as in the example Snap-off).

During imbibition, a decrease in capillary pressure is expected. This causes a decrease in the interfacial fluid/fluid curvature, corresponding to an increase in the radius of curvature (based on the Young Laplace equation). Since the contact angles measured at the resolution of this dataset are the effective contact angles and not the molecular contact angles, the decrease in curvature can explain the increase in geometric contact angles.

In Event 1, the geometric contact angles continue increasing and the curvatures continue decreasing after the event has occurred (Figure 27). The fluid/fluid interface is still present in the pores neighbouring the event, explaining these trends. In Event 2 where geometric contact angles decrease and curvatures

increase after the event has occurred (Figure 30), a relaxation occurred. Parallels can be drawn between this and a Haines jump, where after the interface suddenly surges forwards, there is some relaxation where the curvatures decrease locally due to the redistribution of fluids⁹⁹. This scenario is the inverse of this, where after the sudden movement, curvatures increase locally, which means the measured geometric contact angles decrease by the same reasoning as above. In Event 3 measured geometric contact angles and curvatures stop after the event has occurred (Figure 33). There is no more three-phase-contact-line in the event pores or neighbouring pores as there are no more fluid/fluid interfaces here. All pores involved are filled completely with either brine or oil.

The apparent increase in curvature leading up to the snap-off (Figure 36) could be a resolution effect. At (quasi-)equilibrium, interface mean curvatures should be constant for a given pressure, which means that in a given pore the terminal meniscus and arc menisci should have mean curvatures of the same value. The brine layers in corners or roughness are very small in size, and as such have a high curvature in a particular orientation. One principle radius of curvature is on the order of the throat length, which means that for the arc meniscus to have the same mean curvature as the terminal meniscus, the other principle radius of curvature must be very small. A possible explanation for the increase in curvature leading up to the snap-off event is that a radius of curvature below the resolution will result in curvature measurements which are smaller than they should be as the interface will appear to be 'flatter' than it really is. As the layers swell and the curvature lessens, the principle radii of curvature may increase until both are above the resolution and the actual curvature can be measured, explaining why the curvatures may appear low at first and then increase.

5.2.2. Surface areas

Leading up to the events, the rock/brine surface areas increased, while the rock/oil surface areas decreased in each case study. This is exactly what we expected, as brine displaced the oil during imbibition. All the event neighbourhoods have shown some amount of oil/brine interface before the event occurred. This is due to small water layers in the corners or roughness. The oil/brine surface area stayed fairly constant even as the event occurred and then decreased, sometimes dropping to zero. The constant behaviour is because the interfaces between the small water layers and the oil (arc menisci) were replaced with the interface of the terminal menisci as the brine flooded the pores. The decrease in oil/brine surface area occurred when some/all of the pores became completely brine-filled, eliminating oil/brine surface area in that region. When the oil/brine surface area became zero, the oil had been completely displaced from the event neighbourhood (such as in Event 1, Figure 28 and Event 3, Figure 34), at least at the resolution of the images. When the oil/brine surface area dropped to zero, there was no more interface on which to make measurements. The interfacial areas dropping to zero correspond to no more measurements of geometric contact angle or curvature, further validating these measurements as they align with the behaviour of the surface areas.

5.3. Pore filling statistics

5.3.1. Event overview

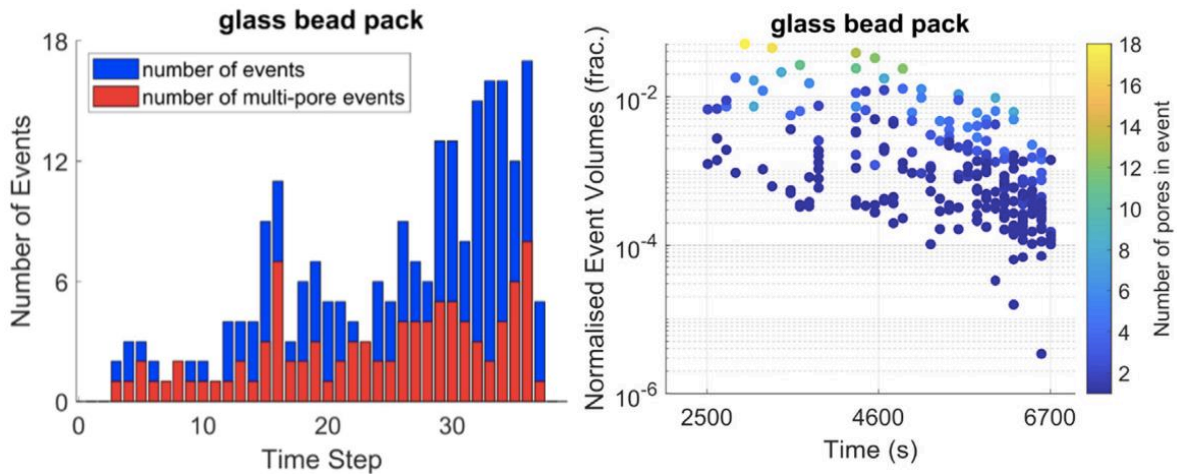


Figure 53: Left: The number of events per timestep for drainage. Right: Normalised event volumes during drainage. Both figures were taken from Mascini et al.¹⁴.

During drainage, larger, well-connected pores were filled first while smaller, more poorly connected pores were filled later in the sequence¹⁴. This is seen by the number of events per timestep increasing as the experiment continues and the volumes of the events decreasing as the experiment continues (Figure 53). So, there were fewer events earlier in the experiments, but these events were larger in size. These trends are very distinct in the above graphs.

During imbibition, however, Figure 38 shows that there were more events per timestep at earlier stages of the experiment, though the trend is not as clear as that seen in the drainage figure. Figure 44 shows a clustering of smaller events at the earlier stages of imbibition, but no clear trends. This suggests that there were more events earlier in the experiment, but that these events were smaller in size. This corresponds with what is known of imbibition, where events occur sequentially, with events which can occur at higher capillary pressures (fillings of pores with smaller radii) happening first.

Piston-like fillings (I_1 events) occur at higher pressures, theoretically making them more favourable, yet I_2 events have had the highest prevalence (Figure 39). This can be due to the nature of the pore space, which in this case is highly connected. Also, what was detected as an I_2 event could in fact have been a snap-off coupled with a piston-like filling, but due to temporal resolution constraints this may not have been resolved. This idea holds for all the higher numbered I_n events. Their high prevalence could be due in part to temporal resolution, where multiple events could be classified as a single event when they occur at timescales smaller than the temporal resolution. Another reason for the unexpectedly large amount of high numbered I_n events could be the way the I_n type was calculated. It was calculated for the entire event volume, not for individual pores, as is the conventional definition. Single-pore events do not suffer from this effect. The trend of the I_n types of the latter (Figure 39) mimics the trends for all the events. This would suggest that it was rather the highly connected nature of the pore space coupled with temporal resolution effects (which could mask snap-offs) that caused the occurrence of many higher numbered I_n events.

5.3.2. Global curvatures and event pressures

The clipped, weighted and then averaged curvatures show a decrease as the experiment proceeds (Figure 41). The reason for this is the same as that in the section Geometric contact angles and curvatures for Case studies of single events. As the pressure decreases, the fluid/fluid interface moves slightly to locations

where equilibrium can again be reached, and this presents itself as the flattening of interfaces. Negative curvatures indicate that the brine is bulging into the oil. While this is possible, it is unlikely to occur so often for water-wet systems and the high occurrence of these negative curvatures is likely due to the formation of pendular rings. Pendular rings are small layers of water that accumulate where the glass beads touch each other or come close to touching (Figure 54). Because they are so small, they are highly sensitive to segmentation error which can cause the improper reversal of curvature values (as described by Armstrong et al.⁵⁷). Further work should be done to identify which negative curvatures are due to pendular rings and to remove those values from further analyses, in particular from the calculation of capillary pressures based on curvature measurements, as done by Armstrong et al.⁵⁷. Not all the negative curvatures can be discarded, as the swelling of water layers can cause arc menisci to bulge slightly into the oil phase, producing negative curvatures which are physical.

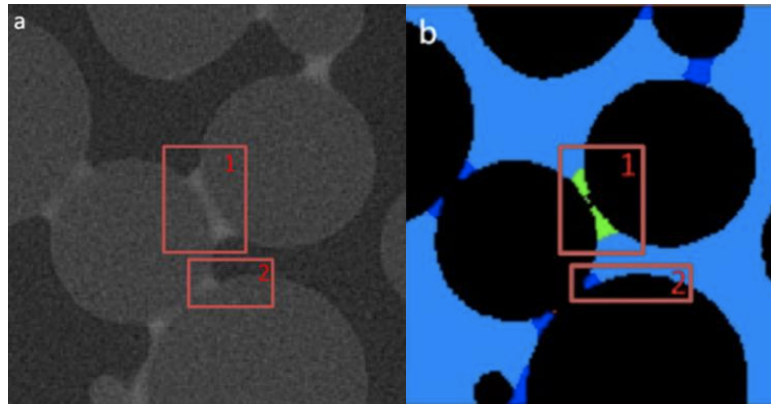


Figure 54: a) Grey-scale image of a glass bead pack during an imbibition experiment. b) The same image segmented. Black is the solid, light blue is the oil, dark blue is the connected water phase and green is the disconnected water phase. Region 1 shows a pendular ring. Due to errors in segmentation, the curvature of the pendular ring is incorrect. The images are taken from Armstrong et al.⁵⁷.

Figure 42 shows that the curvature-derived capillary pressures are mostly in good agreement with the experimental pressures. The deviation where curvature-derived pressures became slightly negative could be explained by the likely errors due to pendular rings. The capillary pressures derived from the model developed by Ruspini et al.⁹⁸ matched the experimental pressures well for piston-like events (where the model reduces to the conventional Young Laplace equation), but produced solely negative pressures for events of type I_2 or higher. Upon further investigation, the model needs adjusting for systems with relatively high contact angles (below 90°), as is the case in our system (72°). The geometric simplifications in the model make cooperative pore filling for these contact angles highly unlikely, which does not seem to reflect the experiment. Further investigation is necessary to investigate whether this is due to the model uncertainty or due to misidentification of snap-off followed by piston-like pore filling as $I_{n \geq 2}$ events in the experiment. Grouping the curvature-based pressures based on event I_n type (Figure 43) shows no clear correlations or trends, even though based on theory, we expect the higher I_n events to have occurred at lower pressures.

5.3.3. Comparison of different types of contact angles

All three different types of contact angles show a positive trend (Figure 46) when plotted against time. The thermodynamic contact angles have a very wide range while the force-based and geometric event-based have narrower ranges. The geometric event-based contact angle has the narrowest range, having only a 15° difference from the smallest to the largest value. This is markedly narrower than its 'static' counterpart, the global geometric contact angles. This shows that the surprisingly large distributions of contact angles reported in the literature are due to the methods of measurement not capturing the dynamics of fluid displacement. These dynamics can include interface relaxation, the location of the contact line at the time

of fluid redistribution, contact angle hysteresis, etc¹⁴. The thermodynamic contact angles show the widest range at the start of imbibition. This is likely due to errors in rock/brine surface area calculations as the smallest pores are invaded first. There is no clear correlation between the I_n event type and the event-based geometric contact angles (Figure 47).

5.4. Comparison between imbibition and drainage

The mechanism of piston-like fillings is most directly comparable to drainage displacements, hence the saturations at the time piston-like events occurred were plotted against the saturations at the times that the same pores were filled during drainage (Figure 50). There is a clear negative trend in this graph, showing that pores filled early in the experiment during drainage were filled late during imbibition (as low invading fluid saturation indicates an earlier stage of the experiment). This aligns with the conventional knowledge that large pores are filled first in drainage and subsequently filled last during imbibition, while small pores are filled last during drainage and first during imbibition.

In the contact angle hysteresis model formulated by Morrow⁴⁵, the advancing contact angles (imbibition contact angles) for a given intrinsic (static) contact angle are higher than the corresponding receding contact angle (drainage contact angle). The graphs in Figure 49 are in agreement with this, as all the points plot above the 1:1 reference line, showing the imbibition contact angles are always higher than the drainage contact angles. This phenomenon is mainly caused by surface roughness¹⁹.

The smallest hysteresis was between the global geometric contact angle measurements of imbibition and drainage (Table 3), while the largest hysteresis was between the thermodynamic contact angle measurements of imbibition and drainage. The distributions of contact angles during drainage can be seen in Figure 55. The hysteresis of particular interest is that of the geometric event-based contact angles, which was 8°. This method takes into account the dynamic nature of fluid displacements coupled with the well-established method of geometric contact angle measurement. Morrow⁴⁵ found a contact angle hysteresis of 12° ($\pm 5^\circ$) for PTFE tubes. The hysteresis seen by Morrow may be comparable to that seen in the glass bead pack as both materials are fairly smooth and indeed the values for hysteresis are similar. During drainage, the mean force-based contact angle differed from the geometric event-based contact angle by 1°, whereas during imbibition the force-based contact angle differed from the geometric event-based contact angle by 9° (which is greater than the hysteresis of the geometric event-based contact angles). This large difference is likely due to the small number of force-based measurements during imbibition, since these values could only be calculated for piston-like events. The standard deviation of the global geometric and geometric event-based contact angles during imbibition were 10.9° and 2.6° respectively, while during drainage these were 9.8° and 2.7°, showing the spreads of these values to be similar between imbibition and drainage. The standard deviation of the force-based and thermodynamic contact angles during imbibition were 9.5° and 23.8° respectively, while during drainage these were 5.3° and 17.9°. This shows that for imbibition, these methods of contact value determination yielded wider distributions. A possible reason is that force-based contact angles could only be calculated for piston-like fillings in imbibition, hence there were far fewer measurements than for drainage.

Table 3: Summary of mean contact angles during imbibition and drainage

	Imbibition	Drainage	Hysteresis
Mean global geometric contact angle	70°	68°	2°
Mean geometric event-based contact angle	72°	64°	8°
Mean force-based contact angle	81°	63°	18°
Mean thermodynamic contact angle	85°	48°	37°

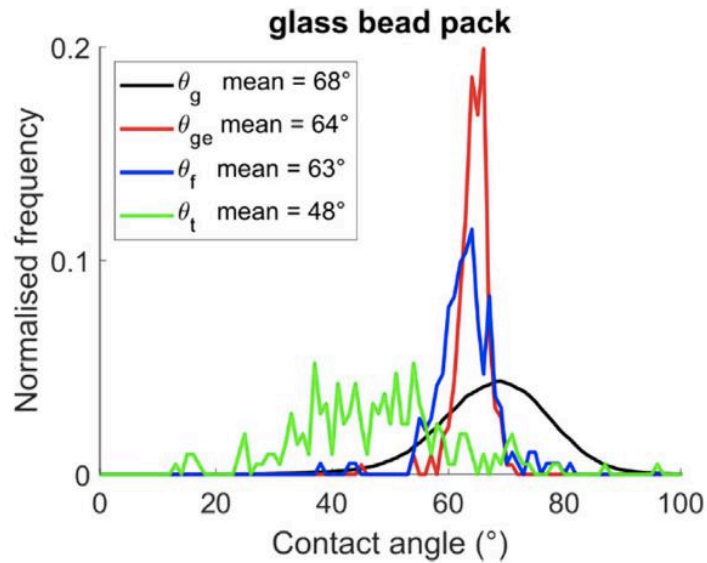


Figure 55: Frequency distributions of different types of contact angles during drainage, taken from Mascini et al.¹⁴. The different types of contact angles are force-based (θ_f), thermodynamic (θ_t), event-based geometric (θ_{ge}) and global geometric (θ_g) contact angles.

During drainage, the trends of the geometric event-based and force-based contact angles remained flat (Figure 56), while during imbibition they showed an increase with time. The trend seen during imbibition was explained by the drop in pressure and subsequent drop in curvature causing the measured contact angles to be higher. By this logic, the pressure increase during drainage should cause the curvatures to increase and the measured contact angles to be lower, but this is not the case. A possible reason for this is that the variations in capillary pressures during imbibition are subtle, making the measured contact angles prone to errors, but this should be further investigated. During drainage, the thermodynamic contact angles have a wider range towards the end of the experiment, while during drainage, the range is wider at the start of the experiment. This is because smaller pores are invaded later during drainage, so errors in the calculation of rock/brine surface areas and fluid/fluid interface curvatures become larger later in the experiment, due to resolution effects.

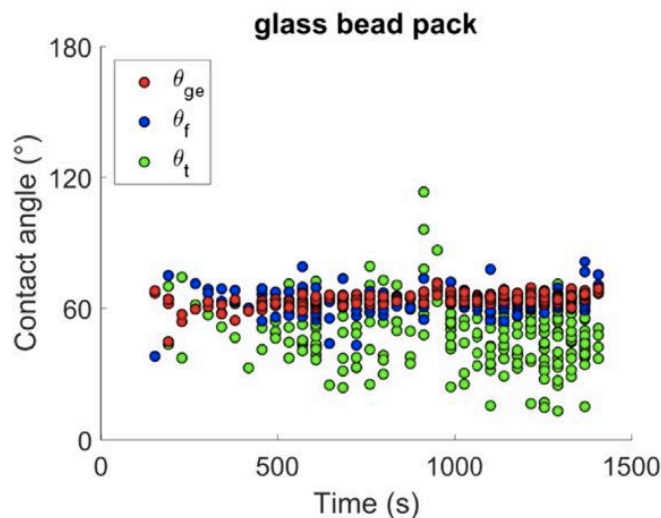


Figure 56: Contact angles plotted against time. The different types of contact angles are force-based (θ_f), thermodynamic (θ_t) and event-based geometric (θ_{ge}) contact angles, taken from Mascini et al.¹⁴.

Together, the capillary pressure curves of drainage and imbibition for the curvature-based pressures and the experimentally derived pressures form a typical example of the classic drainage-imbibition capillary pressure curve (Figure 48). Capillary pressure hysteresis is clearly visible as the capillary pressure for the same saturation during imbibition was lower than during drainage. Some trapping of the oil phase must occur as the saturation at the end of imbibition was close to 0.7, which is lower than the value at the start of drainage, which was almost 1. Based on visualisations of the pore space at the end of imbibition, most of the trapped oil was at the edges of the sample, where the glass beads meet the quartz glass cylinder. This is likely due to the pores in this region having a larger radius than the rest of the pore space. The average contribution to capillary pressure hysteresis purely based on contact angle hysteresis (using geometric event-based contact angle means) is 85 Pa, assuming radius remains constant. This was determined by using the average of the inverse of the radius from the pore or throat that the event originated from, coupled with the Young-Laplace equation. The average capillary pressure hysteresis based on curvature-based pressures was 279 Pa. This means that contact angle hysteresis appears to account for 30% of the hysteresis seen in the capillary pressure.

6. Conclusion

In this dissertation, a time-resolved μ CT dataset of an imbibition experiment was analysed to investigate whether it is possible to measure event-based and force-based contact angles for imbibition and to investigate contact angle hysteresis. Fluid displacement events were detected and classified based on the local fluid configuration. The properties of these events (such as event-based contact angles, event volumes, event curvatures, etc.) were analysed to investigate pore-scale wettability and the impact it has on fluid displacements in imbibition.

Mascini et al.¹⁴ introduced force-based contact angles to link contact angles to the capillary pressures at which displacement events occur. In imbibition, their method is only valid for I_1 events. To extend this to events of I_2 type and higher, the model developed by Ruspini et al.⁹⁸ was used to calculate equivalent threshold capillary pressures. The derived pressures were all negative, begging the question of why these theoretically highly unfavourable events still occurred in the experiment. Further work needs to be done to answer this question or to improve the model. This dissertation, to the best of my knowledge, is the first work to conduct such an in-depth analysis of pore-by-pore filling events identified in experimental imbibition data.

In the case-studies of individual pore-filling events described in this dissertation, the geometric contact angles increased with time, while the curvatures decreased. This was due to the decreasing capillary pressures during imbibition. The geometric event-based contact angles showed this same positive trend with time. The distribution of the geometric event-based contact angles was narrower than the other types of contact angles and also much narrower than its 'static' counterpart: the conventionally calculated geometric contact angles measured everywhere in the pore space on a single image. This aligns with the findings of Mascini et al.¹⁴ on drainage datasets. It shows that for imbibition, the 'static' geometric contact angles do not capture the dynamic nature of fluid interface displacement, resulting in unexpectedly wide distributions of contact angles.

Contact angle hysteresis was evident in all the types of contact angles. This hysteresis ranged from 37° for the mean thermodynamic contact angles to 2° for the mean global geometric contact angles. Geometric event-based contact angles were consistently higher during imbibition than during drainage on a pore-by-pore basis, agreeing with the well-known advancing and receding contact angle versus intrinsic contact angle relation by Morrow⁴⁵: the mean value changed from 64° during drainage to 72° during imbibition,

yielding a hysteresis of 8° . The differences between imbibition and drainage show that for exactly the same porous media, different advancing and receding contact angles occur, showing the effective contact angle is dependent on the saturation path. The measurements indicated that contact angle hysteresis contributed significantly (30%) to the overall average capillary pressure hysteresis. The experiments also showed other forms of hysteresis between drainage and imbibition. The trends of the event-based contact angles with time were positive in the imbibition dataset. In the drainage dataset however, the data trend remained either flat (as in the geometric event-based and force-based contact angles) or was negative (as in the thermodynamic contact angles).

This thesis shows that event-based contact angles can be used to study the link between contact angles and fluid dynamics during imbibition. This is important because imbibition at the pore scale is still not fully understood, making it difficult to model. There is, however, further work to be done: conducting the same analyses on complex samples (such as a natural porous material or mixed-wet case), calculating force-based contact angles for l_2 and higher events and using datasets with a higher temporal resolution. Understanding wettability will help us understand how fluids flow through permeable materials, an essential process to society at large. It will aid in our efforts of combatting climate change, providing fresh water to all and meeting the energy storage demands of the future, not to mention the role multiphase fluid flow plays in countless industrial applications, such as fuel cells or ink spreading on paper.

References

1. Lackner, K. S. A Guide to CO₂ Sequestration. *Science* (80-.). **300**, 1677–1678 (2003).
2. Benson, S. M. & Cole, D. R. CO₂ sequestration in deep sedimentary formations. *Elements* **4**, 325–331 (2008).
3. Bui, M. *et al.* Carbon capture and storage (CCS): The way forward. *Energy Environ. Sci.* **11**, 1062–1176 (2018).
4. Veldkamp, T. I. E. *et al.* Water scarcity hotspots travel downstream due to human interventions in the 20th and 21st century. *Nat. Commun.* **8**, (2017).
5. Stagge, J. H., Kingston, D. G., Tallaksen, L. M. & Hannah, D. M. Observed drought indices show increasing divergence across Europe. *Sci. Rep.* **7**, 1–10 (2017).
6. Hanel, M. *et al.* Revisiting the recent European droughts from a long-term perspective. *Sci. Rep.* **8**, 1–11 (2018).
7. Fetter, C. *Contaminant Hydrogeology*. (Prentice Hall, 1999).
8. Schlüter, S. *et al.* Pore-scale displacement mechanisms as a source of hysteresis for two-phase flow in porous media. *Water Resour. Res.* **52**, 2194–2205 (2016).
9. Singh, K., Bultreys, T., Raeini, A., Shams, M. & Blunt, M. Imbibition in porous media: correlations of displacement events with pore-throat geometry and the identification of a new type of pore snap-off. 1–12 (2019) doi:10.31223/osf.io/62gfr.
10. Zhao, B., MacMinn, C. W. & Juanes, R. Wettability control on multiphase flow in patterned microfluidics. *Proc. Natl. Acad. Sci. U. S. A.* **113**, 10251–10256 (2016).
11. Drelich, J., Miller, J. D. & Good, R. J. The effect of drop (bubble) size on advancing and receding contact angles for heterogeneous and rough solid surfaces as observed with sessile-drop and captive-bubble techniques. *J. Colloid Interface Sci.* **179**, 37–50 (1996).
12. Khishvand, M., Alizadeh, H. A., Oraki Kohshour, I., Piri, M. & Prasad, R. S. In situ characterization of wettability alteration and displacement mechanisms governing recovery enhancement due to low-salinity waterflooding. *Water Resour. Res.* **53**, 4427–4443 (2017).
13. AlRatrou, A., Raeini, A. Q., Bijeljic, B. & Blunt, M. J. Automatic measurement of contact angle in pore-space images. *Adv. Water Resour.* **109**, 158–169 (2017).
14. Mascini, A., Cnudde, V. & Bultreys, T. Event-based contact angle measurements inside porous media using time-resolved micro-computed tomography. *J. Colloid Interface Sci.* **572**, 354–363 (2020).
15. Blunt, M. J., Lin, Q., Akai, T. & Bijeljic, B. A thermodynamically consistent characterization of wettability in porous media using high-resolution imaging. *J. Colloid Interface Sci.* **552**, 59–65 (2019).
16. Basirat, F., Yang, Z. & Niemi, A. Pore-scale modeling of wettability effects on CO₂-brine displacement during geological storage. *Adv. Water Resour.* **109**, 181–195 (2017).
17. Hashemi, L., Blunt, M. & Hajibeygi, H. Pore-scale modelling and sensitivity analyses of hydrogen-brine multiphase flow in geological porous media. *Sci. Rep.* **11**, 1–13 (2021).
18. Sun, C. *et al.* Probing Effective Wetting in Subsurface Systems. *Geophys. Res. Lett.* **47**, (2020).
19. Blunt, M. J. Multiphase Flow in Permeable Media. *Multiphase Flow in Permeable Media* (2017) doi:10.1017/9781316145098.
20. Quéré, D. Wetting and roughness. *Annu. Rev. Mater. Res.* **38**, 71–99 (2008).
21. Levine, S., Bowen, B. D. & Partridge, S. J. Stabilization of emulsions by fine particles II. capillary and van der Waals forces between particles. *Colloids and Surfaces* **38**, 345–364 (1989).
22. Vavra, C. L., Kaldi, J. G. & Sneider, R. M. Geological Applications of Capillary Pressure: A Review. *Am. Assoc. Pet. Geol. Bull.* **76**, 840–850 (1992).
23. Li, T., Schlüter, S., Dragila, M. I. & Wildenschild, D. An improved method for estimating capillary pressure from 3D microtomography images and its application to the study of disconnected

- nonwetting phase. *Adv. Water Resour.* **114**, 249–260 (2018).
24. Armstrong, R. T., Evseev, N., Koroteev, D. & Berg, S. Modeling the velocity field during Haines jumps in porous media. *Adv. Water Resour.* **77**, 57–68 (2015).
 25. Juanes, R., Spiteri, E. J., Orr, F. M. & Blunt, M. J. Impact of relative permeability hysteresis on geological CO₂ storage. *Water Resour. Res.* **42**, 1–13 (2006).
 26. Andrew, M., Menke, H., Blunt, M. J. & Bijeljic, B. The Imaging of Dynamic Multiphase Fluid Flow Using Synchrotron-Based X-ray Microtomography at Reservoir Conditions. *Transp. Porous Media* **110**, (2015).
 27. Roof, J. G. Snap-Off of Oil Droplets in Water-Wet Pores. *Soc. Pet. Eng. J.* **10**, 85–90 (1970).
 28. Liu, Y., Iglauer, S., Cai, J., Amooie, M. A. & Qin, C. Local instabilities during capillary-dominated immiscible displacement in porous media. *Capillarity* **2**, 1–7 (2019).
 29. Berg, S. *et al.* Connected pathway relative permeability from pore-scale imaging of imbibition. *Adv. Water Resour.* **90**, 24–35 (2016).
 30. Valvatne, P. H. & Blunt, M. J. Predictive pore-scale modeling of two-phase flow in mixed wet media. *Water Resour. Res.* **40**, 1–21 (2004).
 31. Lenormand, R., Zarcone, C. & Sarr, A. Mechanisms of the displacement of one fluid by another in a network of capillary ducts. *J. Fluid Mech.* **135**, 337 (1983).
 32. Singh, K., Jung, M., Brinkmann, M. & Seemann, R. Capillary-dominated fluid displacement in porous media. *Annu. Rev. Fluid Mech.* **51**, 429–449 (2019).
 33. Joekar-Niasar, V., Doster, F., Armstrong, R. T., Wildenschild, D. & Celia, M. A. Trapping and hysteresis in two-phase flow in porous media: A pore-network study. *Water Resour. Res.* **49**, 4244–4256 (2013).
 34. Tahmasebi, P. & Kamrava, S. Rapid multiscale modeling of flow in porous media. *Phys. Rev. E* **98**, 1–13 (2018).
 35. McClure, J. E. *et al.* Geometric state function for two-fluid flow in porous media. *Phys. Rev. Fluids* **3**, 1–11 (2018).
 36. Plug, W.-J. & Bruining, J. Capillary pressure for the sand–CO₂–water system under various pressure conditions. Application to CO₂ sequestration. *Adv. Water Resour.* **30**, 2339–2353 (2007).
 37. Spiteri, E. J., Juanes, R., Blunt, M. J. & Orr, F. M. A new model of trapping and relative permeability hysteresis for all wettability characteristics. *SPE J.* **13**, 277–288 (2008).
 38. Jackson, S. J., Lin, Q. & Krevor, S. Representative Elementary Volumes, Hysteresis, and Heterogeneity in Multiphase Flow From the Pore to Continuum Scale. *Water Resour. Res.* **56**, 1–24 (2020).
 39. Land, C. S. Calculation of Imbibition Relative Permeability for Two- and Three-Phase Flow From Rock Properties. *Soc. Pet. Eng. J.* **8**, 149–156 (1968).
 40. Carlson, F. M. Simulation of Relative Permeability Hysteresis To the Nonwetting Phase. *Soc. Pet. Eng. AIME, SPE* (1981) doi:10.2118/10157-ms.
 41. Lenhard, R. J. & Parker, J. C. A Model for Hysteretic Constitutive Relations Governing Multiphase Flow 2. Permeability-Saturation Relations. *Water Resour. Res.* **23**, 2197–2206 (1987).
 42. Jerauld, G. R. General Three-Phase Relative Permeability Model for Prudhoe Bay. *SPE Reserv. Eng. (Society Pet. Eng.)* **12**, 255–263 (1997).
 43. Larsen, J. A. & Skauge, A. Methodology for Numerical Simulation with Cycle-Dependent Relative Permeabilities. *SPE J.* **3**, 163–173 (1998).
 44. Blunt, M. J. An empirical model for three-phase relative permeability. *SPE J.* **5**, 435–445 (2000).
 45. Morrow, N. R. The Effects of Surface Roughness On Contact: Angle With Special Reference to Petroleum Recovery. *J. Can. Pet. Technol.* **14**, (1975).
 46. Anbari, A. *et al.* Microfluidic Model Porous Media: Fabrication and Applications. *Small* **14**, (2018).
 47. Lenormand, R., Touboul, E. & Zarcone, C. Numerical models and experiments on immiscible displacements in porous media. *J. Fluid Mech* **189**, 165–187 (1988).

48. Lenormand, R. & Zarcone, C. Role of roughness and edges during imbibition in square capillaries. *Proc. - SPE Annu. Tech. Conf. Exhib.* **1984-Septe**, (1984).
49. Lenormand, R. Liquids in porous media. *J. Phys. Condens. Matter* **2**, SA79–SA88 (1990).
50. Cieplak, M. & Robbins, M. O. Dynamical transition in quasistatic fluid invasion in porous media. *Phys. Rev. Lett.* **60**, 2042–2045 (1988).
51. Cieplak, M. & Robbins, M. O. Influence of contact angle on quasistatic fluid invasion of porous media. *Phys. Rev. B* **41**, 11508–11521 (1990).
52. Martys, N., Cieplak, M. & Robbins, M. O. Critical phenomena in fluid invasion of porous media. *Phys. Rev. Lett.* **66**, 1058–1061 (1991).
53. Chraïbi, H., Prat, M. & Chapuis, O. Influence of contact angle on slow evaporation in two-dimensional porous media. *Phys. Rev. E* **79**, 1–33 (2009).
54. Krummel, A. T., Datta, S. S., Münster, S. & Weitz, D. A. Visualizing multiphase flow and trapped fluid configurations in a model three-dimensional porous medium. *AIChE J.* **59**, 1022–1029 (2013).
55. Hazlett, R. D. Simulation of capillary-dominated displacements in microtomographic images of reservoir rocks. *Transp. Porous Media* **20**, 21–35 (1995).
56. Murison, J., Moosavi, R., Schulz, M., Schillinger, B. & Schröter, M. Neutron Tomography as a Tool to Study Immiscible Fluids in Porous Media without Chemical Dopants. *Energy and Fuels* **29**, 6271–6276 (2015).
57. Armstrong, R. T., Porter, M. L. & Wildenschild, D. Linking pore-scale interfacial curvature to column-scale capillary pressure. *Adv. Water Resour.* **46**, 55–62 (2012).
58. Andrew, M., Bijeljic, B. & Blunt, M. J. Pore-scale contact angle measurements at reservoir conditions using X-ray microtomography. *Adv. Water Resour.* **68**, 24–31 (2014).
59. Lv, P. *et al.* In Situ Local Contact Angle Measurement in a CO₂-Brine-Sand System Using Microfocused X-ray CT. *Langmuir* **33**, 3358–3366 (2017).
60. Lv, P., Liu, Y., Jiang, L., Song, Y. & Huang, Q. Pore-scale contact angle measurements of CO₂-brine-glass beads system using micro-focused X-ray computed tomography. *Micro Nano Lett.* **11**, 524–527 (2016).
61. Jafari, M. & Jung, J. Direct measurement of static and dynamic contact angles using a random micromodel considering geological CO₂ sequestration. *Sustain.* **9**, (2017).
62. Dalton, L. E., Klise, K. A., Fuchs, S., Crandall, D. & Goodman, A. Methods to measure contact angles in scCO₂-brine-sandstone systems. *Adv. Water Resour.* **122**, 278–290 (2018).
63. Tudek, J. *et al.* In situ contact angle measurements of liquid CO₂, brine, and Mount Simon sandstone core using micro X-ray CT imaging, sessile drop, and Lattice Boltzmann modeling. *J. Pet. Sci. Eng.* **155**, 3–10 (2017).
64. Singh, K., Bijeljic, B. & Blunt, M. J. Imaging of oil layers, curvature and contact angle in a mixed-wet and a water-wet carbonate rock. *Water Resour. Res.* **52**, 1716–1728 (2016).
65. Scanziani, A., Singh, K., Blunt, M. J. & Guadagnini, A. Automatic method for estimation of in situ effective contact angle from X-ray micro tomography images of two-phase flow in porous media. *J. Colloid Interface Sci.* **496**, 51–59 (2017).
66. Alhammadi, A. M., Alratrout, A., Singh, K., Bijeljic, B. & Blunt, M. J. In situ characterization of mixed-wettability in a reservoir rock at subsurface conditions. *Sci. Rep.* **7**, 1–9 (2017).
67. Klise, K. A., Moriarty, D., Yoon, H. & Karpyn, Z. Automated contact angle estimation for three-dimensional X-ray microtomography data. *Adv. Water Resour.* **95**, 152–160 (2016).
68. Ibekwe, A., Pokrajac, D. & Tanino, Y. Automated extraction of in situ contact angles from micro-computed tomography images of porous media. *Comput. Geosci.* **137**, 104425 (2020).
69. Scanziani, A., Singh, K., Bultreys, T., Bijeljic, B. & Blunt, M. J. In situ characterization of immiscible three-phase flow at the pore scale for a water-wet carbonate rock. *Adv. Water Resour.* **121**, 446–455 (2018).
70. AlRatrou, A., Blunt, M. J. & Bijeljic, B. Spatial Correlation of Contact Angle and Curvature in Pore-

- Space Images. *Water Resour. Res.* **54**, 6133–6152 (2018).
71. AlRatrouf, A., Blunt, M. J. & Bijeljic, B. Wettability in complex porous materials, the mixed-wet state, and its relationship to surface roughness. *Proc. Natl. Acad. Sci. U. S. A.* **115**, 8901–8906 (2018).
 72. Armstrong, R. T. *et al.* Subsecond pore-scale displacement processes and relaxation dynamics in multiphase flow. *Water Resour. Res.* **50**, 9162–9176 (2014).
 73. Bultreys, T., De Boever, W. & Cnudde, V. Imaging and image-based fluid transport modeling at the pore scale in geological materials: A practical introduction to the current state-of-the-art. *Earth-Science Rev.* **155**, 93–128 (2016).
 74. Cnudde, V. & Boone, M. N. High-resolution X-ray computed tomography in geosciences: A review of the current technology and applications. *Earth-Science Rev.* **123**, 1–17 (2013).
 75. Armstrong, R. T., Georgiadis, A., Ott, H., Klemin, D. & Berg, S. Critical capillary number: Desaturation studied with fast X-ray computed microtomography. *Geophys. Res. Lett.* **41**, 55–60 (2014).
 76. Rücker, M. *et al.* From connected pathway flow to ganglion dynamics. *Geophys. Res. Lett.* **42**, 3888–3894 (2015).
 77. Chalbaud, C. *et al.* Interfacial tension measurements and wettability evaluation for geological CO₂ storage. *Adv. Water Resour.* **32**, 98–109 (2009).
 78. Seibert, J. A. Part 1: Basic principles of x-ray production. *J Nucl Med Technol* **32**, 139–47 (2004).
 79. Michael, G. X-ray computed tomography. *Phys. Educ.* **36**, 442–451 (2001).
 80. Bonse, U. & Busch, F. X-ray computed microtomography (μ CT) using synchrotron radiation (SR). *Prog. Biophys. Mol. Biol.* **65**, 133–169 (1996).
 81. Cnudde, V. *et al.* Recent progress in X-ray CT as a geosciences tool. *Appl. Geochemistry* **21**, 826–832 (2006).
 82. Vlassenbroeck, J. *et al.* Software tools for quantification of X-ray microtomography at the UGCT. *Nucl. Instruments Methods Phys. Res. Sect. A Accel. Spectrometers, Detect. Assoc. Equip.* **580**, 442–445 (2007).
 83. Lin, Q., Al-Khulaifi, Y., Blunt, M. J. & Bijeljic, B. Quantification of sub-resolution porosity in carbonate rocks by applying high-salinity contrast brine using X-ray microtomography differential imaging. *Adv. Water Resour.* **96**, 306–322 (2016).
 84. Tafforeau, P. *et al.* Applications of X-ray synchrotron microtomography for non-destructive 3D studies of paleontological specimens. *Appl. Phys. A Mater. Sci. Process.* **83**, 195–202 (2006).
 85. Cloetens, P. *et al.* Holotomography: Quantitative phase tomography with micrometer resolution using hard synchrotron radiation x rays. *Appl. Phys. Lett.* **75**, 2912–2914 (1999).
 86. David, C. *et al.* Hard X-ray phase imaging and tomography using a grating interferometer. *Spectrochim. Acta - Part B At. Spectrosc.* **62**, 626–630 (2007).
 87. Stock, S. R. *Microcomputed tomography: methodology and applications.* (CRC Press, 2019).
 88. Ketcham, R. A. Computational methods for quantitative analysis of three-dimensional features in geological specimens. *Geosphere* **1**, 32–41 (2005).
 89. Brabant, L. *et al.* Three-dimensional analysis of high-resolution X-ray computed tomography data with morpho+. *Microsc. Microanal.* **17**, 252–263 (2011).
 90. Schindelin, J. *et al.* Fiji: an open-source platform for biological-image analysis. *Nat. Methods* **9**, 676–682 (2012).
 91. Tristán-Vega, A., García-Pérez, V., Aja-Fernández, S. & Westin, C.-F. Efficient and robust nonlocal means denoising of MR data based on salient features matching. *Comput. Methods Programs Biomed.* **105**, 131–144 (2012).
 92. Rudin, L. I., Osher, S. & Fatemi, E. Nonlinear total variation based noise removal algorithms. *Phys. D Nonlinear Phenom.* **60**, 259–268 (1992).
 93. Shams, M., Raeini, A. Q., Blunt, M. J. & Bijeljic, B. A numerical model of two-phase flow at the

- micro-scale using the volume-of-fluid method. *J. Comput. Phys.* **357**, 159–182 (2018).
94. Bultreys, T. *et al.* Verifying Pore Network Models of Imbibition in Rocks Using Time-Resolved Synchrotron Imaging. *Water Resour. Res.* **56**, (2020).
 95. Raeini, A. Q., Bijeljic, B. & Blunt, M. J. Generalized network modeling of capillary-dominated two-phase flow. *Phys. Rev. E* **97**, (2018).
 96. Lorensen, W. E. & Cline, H. E. Marching cubes: A high resolution 3D surface construction algorithm. *Proc. 14th Annu. Conf. Comput. Graph. Interact. Tech. SIGGRAPH 1987* **21**, 163–169 (1987).
 97. Dijkstra, E. W. A note on two problems in connexion with graphs. *Numer. Math.* **1**, 269–271 (1959).
 98. Ruspini, L. C., Farokhpoor, R. & Øren, P. E. Pore-scale modeling of capillary trapping in water-wet porous media: A new cooperative pore-body filling model. *Adv. Water Resour.* **108**, 1–14 (2017).
 99. Schlüter, S., Berg, S., Li, T., Vogel, H.-J. & Wildenschild, D. Time scales of relaxation dynamics during transient conditions in two-phase flow. *Water Resour. Res.* **53**, 4709–4724 (2017).